Submesoscale Processes at Shallow Salinity Fronts in the Bay of Bengal: Observations during the Winter Monsoon

SANJIV RAMACHANDRAN AND AMIT TANDON

Department of Mechanical Engineering, University of Massachusetts Dartmouth, Dartmouth, Massachusetts

JENNIFER MACKINNON, ANDREW J. LUCAS, ROBERT PINKEL, AND AMY F. WATERHOUSE

Scripps Institution of Oceanography, University of California, San Diego, La Jolla, California

JONATHAN NASH AND EMILY SHROYER

College of Earth, Ocean and Atmospheric Science, Oregon State University, Corvallis, Oregon

AMALA MAHADEVAN, ROBERT A. WELLER, AND J. THOMAS FARRAR

Woods Hole Oceanographic Institution, Woods Hole, Massachusetts

(Manuscript received 20 December 2016, in final form 30 December 2017)

ABSTRACT

Lateral submesoscale processes and their influence on vertical stratification at shallow salinity fronts in the central Bay of Bengal during the winter monsoon are explored using high-resolution data from a cruise in November 2013. The observations are from a radiator survey centered at a salinity-controlled density front, embedded in a zone of moderate mesoscale strain (0.15 times the Coriolis parameter) and forced by winds with a downfront orientation. Below a thin mixed layer, often $\leq$10 m, the analysis shows several dynamical signatures indicative of submesoscale processes: (i) negative Ertel potential vorticity (PV); (ii) low-PV anomalies with $O(1\text{–}10)$ km lateral extent, where the vorticity estimated on isopycnals and the isopycnal thickness are tightly coupled, varying in lockstep to yield low PV; (iii) flow conditions susceptible to forced symmetric instability (FSI) or bearing the imprint of earlier FSI events; (iv) negative lateral gradients in the absolute momentum field (inertial instability); and (v) strong contribution from differential sheared advection at $O(1)$ km scales to the growth rate of the depth-averaged stratification. The findings here show one-dimensional vertical processes alone cannot explain the vertical stratification and its lateral variability over $O(1\text{–}10)$ km scales at the radiator survey.

1. Introduction

The Bay of Bengal receives an enormous amount of freshwater from precipitation and river runoff (Shetye et al. 1996; Sengupta et al. 2006). According to estimates from observations (Dai and Trenberth 2002; Fekete and Vörösmarty 2002; Sengupta et al. 2006), the Bay accounts for more than half of the total continental runoff into the entire tropical Indian Ocean. The Bay is freshest during June–August (Rao and Sivakumar 2003) when both precipitation and the rivers, swollen from the monsoon rains, feed the Bay. This influx of freshwater often creates thin, salinity-stratified layers confined to the upper 20–30 m of the Bay. The consequences of this stratification for vertical exchange have been the focus of much research (Sengupta and Ravichandran 2001; Vinaychandran et al. 2002; Thadathil et al. 2007; Sengupta et al. 2008). Strong stratification near the surface inhibits vertical turbulent transport, thereby limiting the subsurface fluxes of momentum, heat, and tracers (Kumar et al. 2002). The resulting dynamical isolation of the surface layers from the deeper nutrient-rich layers is a key factor explaining the lower biological productivity of the Bay compared to the Arabian Sea on the western coast of India (Kumar et al. 2002). The salinity stratification near the surface allows for strong subsurface temperature inversions (as large as 4°C), a

---

Corresponding author: Sanjiv Ramachandran, sramachandran@umassd.edu

DOI: 10.1175/JPO-D-16-0283.1

defining feature of the Bay during winter (Thadathil et al. 2002). The entrainment of subsurface warm layers prevents the decrease in SST typically associated with mixing during a storm (Sengupta et al. 2008). Vertical mixing of temperature inversions can even achieve a net warming of the upper ocean, which in turn can intensify cyclones through enhanced convective activity (Balaguru et al. 2012).

The role of lateral gradients in salinity has been more challenging to decipher. The influx of freshwater into the Bay not only enhances the vertical stratification but also generates strong horizontal density gradients [$\sim O(1)$ psu] over $O(1\text{–}10)$ km scales (Shetye 1993). As the freshwater plumes get advected offshore and stirred by mesoscale eddies, abundant in the Bay (Gopalan et al. 2000), they create sharp fronts far away from the coast. Indeed, the observations in the present study recorded salinity differences as large as $O(1)$ g kg^{-1} across $O(1)$ km in the central Bay toward the edge of a mesoscale eddy. This region was characterized by a moderately confluent mesoscale strain field, an environment conducive to frontogenesis and submesoscale [$O(1\text{–}10)$ km] instabilities (D'Asaro et al. 2011). The presence of such sharp frontal gradients raises the possibility of an active role for submesoscale processes in the Bay.

Fronts in the mixed layer can host a wide variety of instabilities. In this document, we use the term "frontal instabilities" broadly to refer to such instabilities, which include baroclinic and symmetric instability and other types of instabilities (Arobone and Sarkar 2015). Among the different possible classes of frontal instability, symmetric instability (SI; Taylor and Ferrari 2010; Thomas et al. 2013) and ageostrophic baroclinic instability (ABI; Boccaletti et al. 2007; Capet et al. 2008a; Fox-Kemper et al. 2008) have received considerable attention in observational and numerical studies.[1] Other instabilities such as anticyclonic ageostrophic instability, predicted by linear theory (Molemaker and McWilliams 2005), have been documented in direct numerical simulations (Barkan et al. 2015) but await experimental confirmation. The presence of surface waves introduces complex interactions between fronts and Stokes shear that recent works are beginning to address (McWilliams and Fox-Kemper 2013; Hamlington et al. 2014; Haney et al. 2015).

SI occurs when the Ertel potential vorticity (PV) attains negative values (in the Northern Hemisphere; Hoskins 1974). It is a two-dimensional instability with no variation of properties along the front that extracts energy from the flow by feeding on the geostrophic shear. A flow in geostrophic balance permits SI for values of the balanced Richardson number Ri_B smaller than unity. Downfront winds (aligned with the thermal wind) or surface cooling at a front can continuously extract PV from the water column (Thomas 2005), giving rise to forced symmetric instability (FSI; Thomas et al. 2013). Ageostrophic baroclinic instability converts available potential energy (APE) to kinetic energy (KE) over scales shorter and quicker than those characterizing quasigeostrophic baroclinic instability of the pycnocline. Unlike SI, it persists for $\mathrm{Ri}_B > 1$. Studies suggest ABI and SI can act in concert, such that the latter destroys the KE generated by the former (Thomas et al. 2013). Inertial instability arises from an unstable equilibrium between the Coriolis force and the horizontal pressure gradient force (Holton 1992). A flow in geostrophic balance becomes unstable to inertial instability when the absolute momentum develops negative gradients, or equivalently, the relative vorticity becomes more negative than $-f$ (Haine and Marshall 1998). For balance in the presence of strong flow curvature (cyclostrophic balance), the centrifugal force also contributes significantly to the energetics of inertially unstable motions.

Instabilities at fronts have important consequences for the vertical structure of the upper ocean. Near fronts, both SI and ABI can achieve rapid shallowing of the mixed layer over inertial time scales. Restratification due to geostrophic adjustment and SI can each achieve $\mathrm{Ri}_B \sim O(1)$, while the increase in Ri_B due to ABI is orders of magnitude larger (Tandon and Garrett 1994; Fox-Kemper et al. 2008). Symmetric instability facilitates the dissipation of the KE (and variance) of the large-scale balanced flow by cascading the KE to smaller scales for removal by three-dimensional diabatic processes (Capet et al. 2008b). The shoaling of the mixed layer due to ABI promotes the uptake of nutrients and biological production in the upper ocean (Mahadevan et al. 2008, 2012). These and other important consequences of frontal instabilities have now been well established in the Atlantic and Pacific Oceans (see references above), as well as in marginal seas of the Arctic (Timmermans and Winsor 2013).

The emphasis in the existing literature on frontal instabilities leans toward $O(100)$ m mixed layers in wintertime conditions (Mahadevan and Tandon 2006; Fox-Kemper et al. 2008; D'Asaro et al. 2011; Mahadevan et al. 2012), a natural choice informed by the seasonality of submesoscale flows, which tend to be most vigorous in winter (Callies et al. 2015). Studies of submesoscale processes in shallower mixed layers, typically during

---

[1] We follow the nomenclature of Thomas et al. (2013), wherein "ageostrophic baroclinic instability" describes the three-dimensional instability (unlike SI) of a front where the APE is converted to eddy kinetic energy (Haine and Marshall 1998; Fox-Kemper et al. 2008). This instability is also sometimes referred to as "geostrophic instability" (Haney et al. 2015).

summertime, have been fewer (Pallàs-Sanz et al. 2010a; Shcherbina et al. 2015). For instance, recent simulations of the Gulf of Mexico report energetic submesoscales even in the summer, at fronts formed by the stirring of riverine freshwater (Luo et al. 2016). In the Bay, as in the summertime Gulf of Mexico, submesoscale processes could play a prominent role despite the shallow mixed layers due to the large lateral buoyancy gradients, comparable to strong frontal systems elsewhere (e.g., Kuroshio; D'Asaro et al. 2011; Nagai et al. 2012). A recent study of a yearlong mooring record in the northern Bay (18°N, 89.5°E) reports the frequent passage of $O(1–10)$ km salinity-driven density fronts across the mooring (Sengupta et al. 2016). The study posits submesoscale processes at these fronts might be crucial in maintaining the near-surface stratification from summer through winter. The absence of submesoscale physics in large-scale models could be partly responsible for their excessively deep mixed layers in the northern Bay (Parekh et al. 2016).

In summary, lateral submesoscale processes might potentially be important in the upper Bay, but we know little about them in this region. This is primarily because of the paucity of in situ measurements at scales fine enough to resolve the submesoscales. High-resolution [$O(10)$ km] numerical simulations are starting to explore in detail the three-dimensional structure of salinity and its implications for the upper-ocean circulation in the Bay of Bengal (Benshila et al. 2014), but even such studies only marginally resolve the submesoscales.

In this study, we report and analyze wintertime measurements from a cruise aboard the R/V *Roger Revelle* during 10–27 November 2013. The experiment is part of a larger ongoing international collaboration, Air–Sea Interactions in the Northern Indian Ocean (ASIRI)–Ocean Mixing and Monsoons (OMM; Wijesekera et al. 2016). One of the main goals of ASIRI–OMM is to identify processes that facilitate the cascade of large-scale energy, and temperature and salinity variance to smaller scales, during the summer and winter monsoons. Numerous multiscale surveys during the November 2013 cruise provide a detailed mapping of velocity, temperature, and salinity over lateral scales on the order of 100 m–10 km. The motivation of the present analysis is to investigate the influence of lateral processes at $O(1–10)$ km scales on the vertical stratification in the upper tens of meters in the Bay. To this end, we focus on a high-resolution radiator survey in the central Bay [Central Bay Process Study (CBPS)], lasting approximately a day. The survey was located at a salinity-controlled density front on the edge of a cyclonic mesoscale eddy within a moderately confluent strain field. The winds had a downfront component (aligned with the thermal wind) during most of CBPS. Downfront winds result in the Ekman advection of heavier over lighter fluid, destabilizing the water column (Thomas 2005). An outline of the paper follows.

Section 2 introduces the process study and provides the mesoscale setting for the chosen site. This section also contains a description of the different instruments used in this study and the gridding/interpolation methodology. In section 3 we provide estimates of the relative vorticity and test the flow conditions for geostrophy. In section 4 we assess the relative influence of frictional and diabatic surface forcing on the depth-averaged PV budget, followed by a test of criteria for various frontal instabilities. Section 5 is a discussion of the estimated contributions from vertical and lateral processes to the stratification at CBPS. Section 6 addresses potential contributions from linear internal-wave motions to the observed spatiotemporal variability at the experimental site and describes briefly results from a recent large-eddy simulation (LES) study supporting some of our hypotheses. We summarize our conclusions in section 7.

2. High-resolution frontal process study

a. *Experimental site*

The process study was centered at (16°N, 86.9°E), the choice of location (Fig. 1) guided by (i) precruise images of the sea surface height anomaly (SSHA), (ii) sea surface salinity (SSS) contours, and (iii) surface currents inferred from satellite measurements (details of data sources in section 2b). The site was located toward the outer edge of an $O(100)$ km eddy. The lateral mesoscale strain in this region estimated from the surface currents was $\mathrm{St} = \sqrt{(u_x - v_y)^2 + (u_y + v_x)^2} \approx 0.15f$, where $f = 2\Omega \sin(\gamma)$ is the Coriolis parameter, γ is the latitude, Ω is Earth's rotation rate, u_x is the zonal derivative of the zonal velocity, and so on for the other derivatives.

The survey consists of five transects, nearly parallel (Fig. 1, inset), back and forth across a lens of freshwater. The SSS and surface currents show the larger mesoscale strain field stirring the freshwater entering the survey area. The orientation of the transects is approximately orthogonal to the frontal axis, in order to effectively sample the cross-frontal variability. The length and duration of the transects vary between 25 and 40 km and 2.5 and 6 h, respectively (Table 1). The inertial period at this latitude ($2\pi/f$) is 44 h and the longest transect spans 0.13 inertial periods. As submesoscales evolve on inertial time scales (Thomas et al. 2008), we treat each transect as an independent, instantaneous spatial record to estimate spatial gradients of properties along the ship transect. Earlier studies have used the same approach to

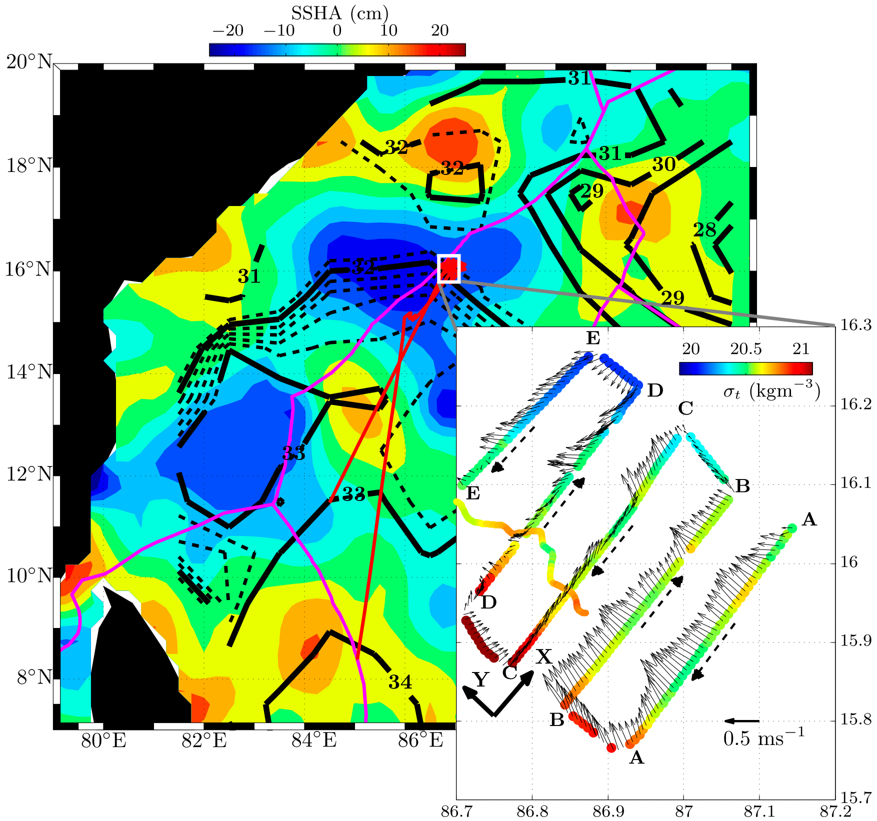

FIG. 1. CCAR SSHA (color) for the week starting 18 Nov 2013 and salinity contours (black solid and dashed; g kg^{-1}) for the week starting 12 Nov 2013 from the level 3.0 Aquarius gridded product version 4.0. The spatial resolution of the CCAR and Aquarius products are 0.25° × 0.25° and 1° × 1°, respectively. The intervals for the solid and dashed contours are 1 and 0.2 g kg^{-1}, respectively. The white box around 16°N identifies the site of a high-resolution radiator survey (inset) at a salinity-driven density front. The inset shows the 1–10-m averaged density (color) from UCTD measurements in tow-yo mode. The five transects (A–E) describe a radiator pattern across a salinity (and density) front. The vectors are the 1-min currents from the SADCP, averaged between 8 and 10 m. The dashed black arrow indicates the ship motion. The curved track cutting across the radiator pattern between 15.9° and 16.1°N shows the position of the WW, drifting freely while profiling between the surface and 150 m. The x and y axes lie along and orthogonal to the transect, respectively. For each transect, the origin is at its southern end.

infer submesoscale gradients from ship-based surveys (Thomas et al. 2010; Hosegood et al. 2013).

We briefly address the possibility of sampling the same water masses in successive transects. For transects A and B, given the direction of ship motion and the upper-ocean currents (Fig. 1), such a possibility is more likely for the northern portions of the two transects. For $23 < x < 26$ km and $-10 < z < -8$ m, the travel time for a water mass from A to B, assuming it advects with the across-track velocity at 8 m [the shallowest reliable depth for the Sentinel V ADCP (SADCP)] orthogonally to transect A, ranges from 7 to 8 h. At other locations, the advection times are longer than 8 h, the combined duration of transects A and B. Hence, we expect minimal advection of water masses from A into B. The across-transect currents decrease from B through E, thus further reducing the potential for this effect in the other transects.

The lower latitude of the experimental site compared to previous frontal studies raises the possibility the

TABLE 1. The length, duration, mean ship speed, and mean orientation for each of the five transects (A–E).

Transect	Length (km)	Duration (h)	Mean ship speed (m s^{-1})	Mean orientation
A	37.16	4.03	2.56	53.4°
B	36.93	4.02	2.55	51.4°
C	39.16	4.54	2.40	53.8°
D	36.78	5.77	1.70	53.4°
E	25.38	2.57	2.74	45.4°

TABLE 2. Instruments are UCTD; SADCP (500 KHz) from RDI Teledyne, deployed on an overboard pole with a transducer depth of 2 m below the surface; PADCP (300 KHz) housed in a well of the ship; Hydrographic Doppler Sonar System (HDSS); and WW (Pinkel et al. 2011). The 75- and 150-KHz ADCPs are mounted on the hull, as is the HDSS. The WW, a freely drifting asset, was deployed on a 150-m-long wire.

Instrument	Temporal resolution (min)	Hor. resolution (km)	Vert. resolution (m)	Depth range (m)
UCTD	7	1.0	1	1–140
SADCP (500KHz)	1	0.14	0.77	5–40
PADCP (300KHz)	1	0.14	3.76	10–60
ADCP (75 and 150KHz)	5	0.71	3	25–150
HDSS (50 and 140KHz)	5	0.71	3	25–150
WW	15	0.14	0.25	10–300

Coriolis terms neglected in the "traditional approximation" might be relevant here. These terms are $-2\Omega w\cos(\gamma)$ in the zonal momentum equation and $2\Omega u\cos(\gamma)$in the vertical momentum equation, respectively. For motions with $O(1)$ Rossby numbers, the neglect of these terms is justified if $|2\Omega\mathcal{H}\cos(\gamma)/\mathcal{U}| \ll 1$, where $\mathcal{H}$ and $\mathcal{U}$ are appropriate scales characterizing the depth and horizontal velocity of motions (White and Bromley 1995). For $\gamma = 16°$N, the above criterion is equivalent to $|\mathcal{H}/\mathcal{U}| \ll 7150$. Using $\mathcal{U} \sim 0.1\,\mathrm{m\,s^{-1}}$ as a representative value, the requirement on $\mathcal{H}$ is easily met as the processes described in this study do not have a vertical scale exceeding 50 m.

b. Data sources

Table 2 lists the resolution (temporal and spatial) and the depth range of the different instruments used in this study. For vertical profiles of temperature and salinity, we use data from (i) underway CTD (UCTD) and (ii) an RBR concerto CTD with lead weights (also referred to as UCTD hereinafter) that profiled from the same winch. Both of these probes were used in "tow-yo" mode during the process-study surveys to enable collection of profiles over the top 100 m every few minutes, which, for a ship speed of $2.5\,\mathrm{m\,s^{-1}}$, is equivalent to a spatial resolution of 0.7–1 km. The Wirewalker wave-powered profiling vehicle (WW), a freely drifting asset, collected profiles of temperature, salinity, velocity, and optical quantities between the surface and 150 m, with an average lateral separation of 0.14 km (depending on drift speed). The WW moved with the depth-averaged flow and therefore was not Lagrangian relative to the flow at any specific isopycnal. The WW measurements began shortly before the commencement of CBPS and continued until after the end of CBPS. As the different ADCPs give consistent results within overlapping depths, whenever possible, we use data from the SADCP (Table 2), which probes shallowest along the water column. We discard SADCP data above 8 m because of noise. When necessary, we combine data from multiple ADCPs to access depths beyond the vertical range of the SADCP. When the SADCP was not deployed, we use a pipestring ADCP (PADCP) housed in a well of the ship.

In generating Fig. 1, we used SSHA from the gridded, weekly altimetry product provided by the Colorado Center for Astrodynamics Research[2] (CCAR; Leben et al. 2002) at a spatial resolution of ¼° × ¼°. We obtain SSS from the gridded data ("level 3" processing) recorded by the NASA Aquarius mission (http://podaac.jpl.nasa.gov/dataset/AQUARIUS_L3_SSS_SMI_7DAY-RUNNINGMEAN_V5; Lee et al. 2012) with a spatial resolution of 1° × 1°. For near-surface currents, we used Ocean Surface Current Analyses Real-Time (OSCAR; https://podaac.jpl.nasa.gov/dataset/OSCAR_L4_OC_third-deg; Bonjean and Lagerloef 2002), which provides estimates of the 0–30-m averaged currents every 5 days at a spatial resolution of ⅓°.

We use the WW to remove the mode-1 baroclinic M_2 tide from the ADCP velocities and the UCTD temperature and salinity fields (appendix A). For all analyses, we use the detided fields.

1) DATA INTERPOLATION, BINNING, AND FILTERING

We perform all interpolation and regridding separately for each transect of the process study. The ADCP measurements have a higher spatial and temporal resolution compared to the UCTD measurements (Table 2). To estimate quantities requiring gradients in both density and velocity, for example, potential vorticity, we interpolate the two fields to a common grid with a uniform horizontal and vertical spacing of 1 km and 1 m, respectively. The grid spans the depths 3–41 m in the vertical. In calculations requiring both density and velocity fields, we only use data from 8 to 41 m.

For all analyses, we align the x and y axes parallel and orthogonal, respectively, to the mean orientation of that transect (Fig. 1). The positive x axis runs northward along a transect. For calculations that combine data

---

[2] The CCAR altimetry product has remained offline since 24 July 2016 because of a breach of the CCAR data servers.

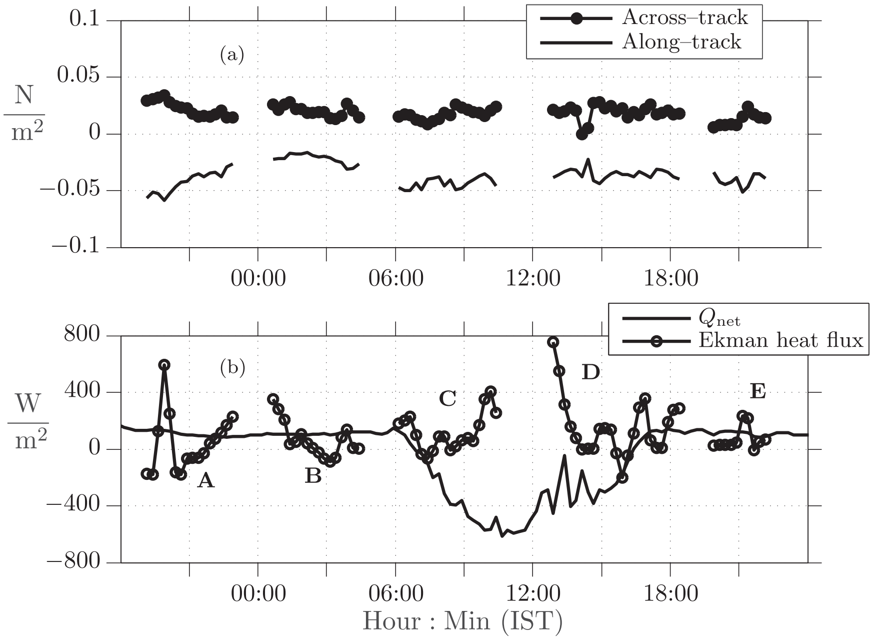

FIG. 2. (a) Wind stresses (N m^{-2}), rotated perpendicular (along front) and parallel (across front) to the transects, approximating the frontal axis to be orthogonal to the transect. The abscissa shows the time in IST. The wind stresses are obtained by applying the COARE 3.0 algorithm to the winds measured at a height of 2 m above the ocean surface. The shipboard meteorological measurements are available every 15 min. (b) Ekman heat flux (Thomas 2005) and Q_{net} (W m^{-2}), where Q_{net} is the algebraic sum of the net shortwave, net longwave, latent, and sensible fluxes, obtained from the TOGA COARE 3.0 algorithm. A positive flux represents the ocean losing heat.

from multiple transects, we ignore the slight variation in the mean orientation from one transect to another.

Most of the calculations use fields smoothed to 8 km at which scale the fields are weakly geostrophic (section 3b). For select calculations, we use finer averaging scales. Unless otherwise stated, it is to be assumed we are using fields smoothed to 8 km. We use a third-order Butterworth filter for all low-pass operations in this study. This filter attenuates the amplitude of the original signal by $1/\sqrt{2}$ (and attenuates power by 1/2) at the cutoff wavelength.

2) METEOROLOGICAL FORCING

We use the TOGA COARE 3.0 algorithm (Fairall et al. 2003) to estimate the surface wind stress τ and the net heat flux Q_{net} from the 15-min shipboard meteorological measurements. The effective spatial resolution of these measurements, using the average ship speed during CBPS, is 2.1 km. We approximate Q_{net} as the algebraic sum of the shortwave, longwave, sensible, and latent fluxes, neglecting any thermal contribution from rainwater. A positive flux indicates cooling of the ocean.

Strong winds and stormy conditions preceded CBPS between 19 and 21 November 2013, with wind stresses approaching 0.2 N m^{-2}. The process study itself, starting 1903 India Standard Time (IST) 22 November and ending 2213 IST 23 November, was marked by clear conditions and considerably weaker wind stress (mean: 0.04 N m^{-2}, maximum: 0.07 N m^{-2}; Fig. 2a). The winds were predominantly northeasterly, typical for the winter monsoon. The process study encountered one complete diurnal cycle of thermal forcing. The magnitude of the maximum heat flux, 600 W m^{-2}, was close to the maximum value over the entire duration of the cruise. Averaged over the duration of CBPS, the ocean received a net heat input of 49 W m^{-2}.

3. Gradients in salinity, temperature, and velocity fields

Lateral density gradients abound in the upper tens of meters for all five transects (Fig. 3), controlled by variations in salinity. For transects A, B, and C, a lens of cold freshwater, approximately 15 km wide and 20 m deep, generates sharp gradients at its edges. During CBPS, the UCTD measurements reported lateral salinity variations as large as 0.6 g kg^{-1} across 1 km, while routinely sampling changes of 0.2 g kg^{-1} across 1 km. These lateral gradients are considerably stronger than those reported in earlier studies of the Bay during this time of the year (e.g., 1 psu across 20 km; Shetye 1993). The survey

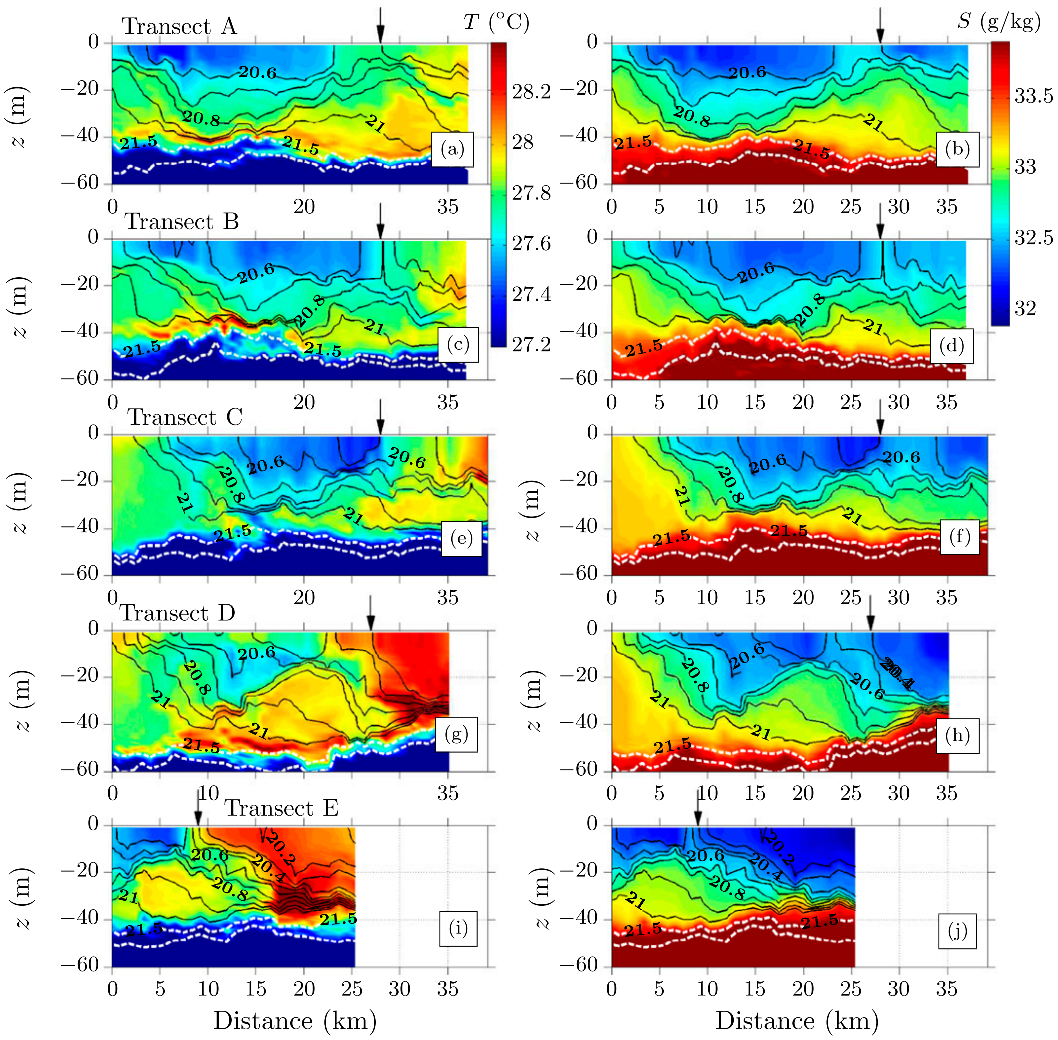

FIG. 3. Sections of the detided (no M_2 contribution) temperature (°C) and salinity ($g\,kg^{-1}$) plotted as a function of the distance traveled by the ship. The x axis in all plots is oriented from southwest ($x = 0$ km) to northeast. The black arrows indicate the location of the frontal axis for each transect (see Fig. 7). The isopycnal contours for the solid and dashed lines are separated by 0.05 and 0.5 $kg\,m^{-3}$, respectively.

shows both compensated and uncompensated fronts. For instance, in transects C and D, the fronts in the upper 20 m appear to be partially compensated between 0 and 10 km, unlike those between 25–35 km. The temperature–salinity (T–S) sections (Fig. 3) and T–S diagrams (not shown) indicate the waters at CBPS comprise at least three distinct water masses. The waters in transect C are warm and salty to the south, cold and fresh in the middle, and warm and fresh farther to the north. The freshwater lenses have advected southward in D and E, which receive an influx of much lighter waters from the north (top-right corner of D and E).

Stratification persists throughout the upper water column, with considerable variability along isopycnals (Fig. 3). In particular, there are several patches of anomalously low stratification along outcropping isopycnals. Salinity variations control the vertical stratification $N^2 = \partial b/\partial z$ over the top 40 m (Fig. 4), where $b = -(g/\rho_0)\rho$ is the buoyancy, ρ is the potential density, $g = 9.8\,m\,s^{-2}$ is the acceleration due to gravity and $\rho_0 = 1027\,kg\,m^{-3}$ is the reference density. The stratification increases sharply below 40 m, with the main pycnocline lying between 40 and 50 m (Fig. 4). Together, the five transects show an abundance of outcropping, salinity-controlled density fronts embedded in weak to moderate stratification.

a. *Vorticity*

The velocity vectors averaged over the top 10 m show a predominantly northwestward flow (Fig. 1). For all five transects, the along-transect velocity u is confluent at the edges over the top 20 m (Fig. 5). For

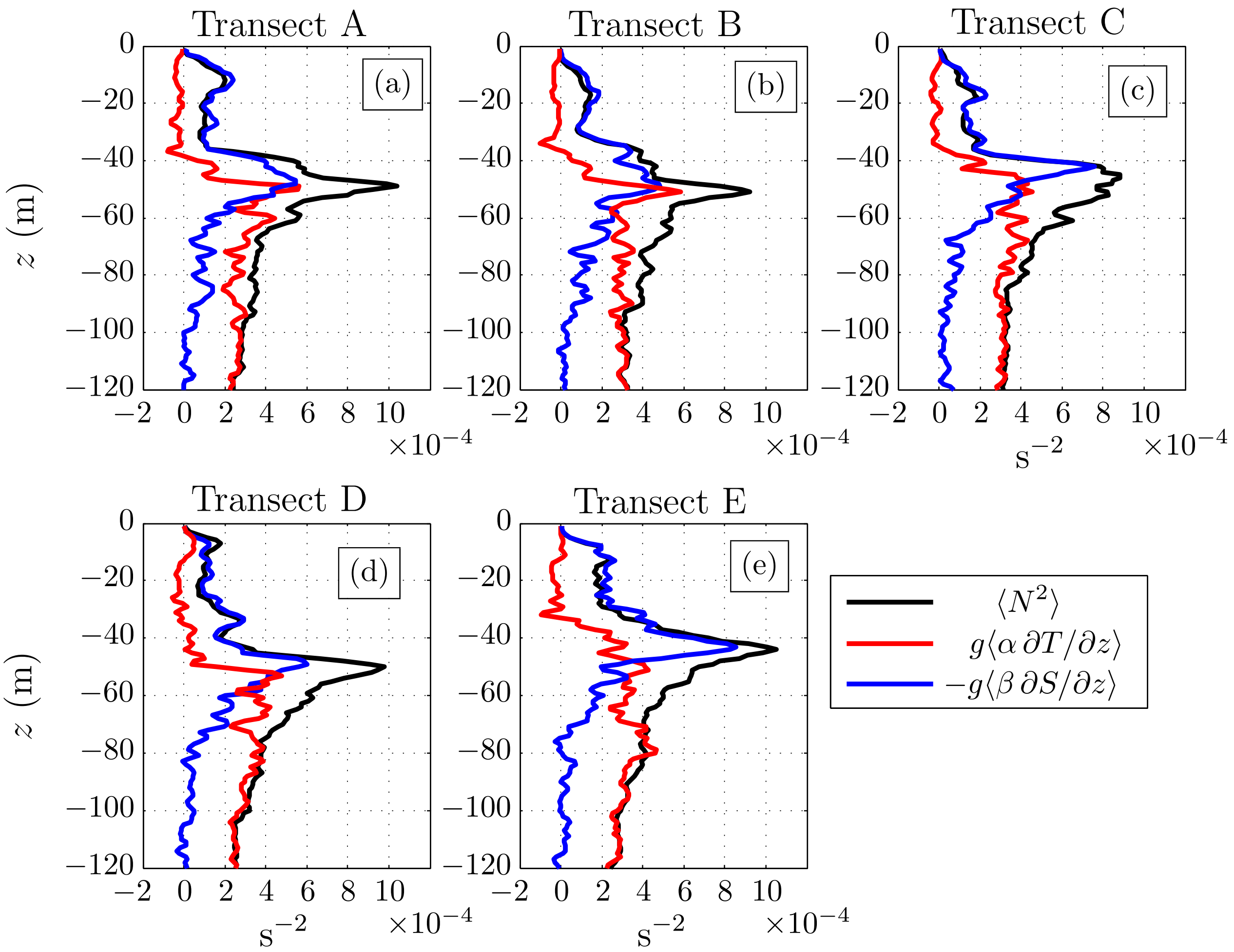

FIG. 4. Vertical stratification, N^2 (s^{-2}; black), for each of the five radiator transects with the contributions from salinity (blue) and temperature (red). The angled brackets represent averaging over the transect at a fixed depth.

instance, this is evident for transect A, where the direction of u changes from northeastward to southwestward along the transect. We quantify the strength of confluence in later discussions (section 5a). The velocity orthogonal to the transects v is strongest within the top 20 m.

We use the so-called "one ship" approximation (Shcherbina et al. 2013), wherein we use the along-track gradients of the across-track velocity $\zeta \approx \partial v/\partial x$ to obtain the vertical vorticity. An important caveat here is that this approximation, in comparison with ζ estimated from simultaneous two-ship measurements, predicts a more symmetric probability distribution of ζ with a near-zero mode and lower skewness (Shcherbina et al. 2013).

To illustrate the effect of scale on vorticity, we plot ζ from one of the transects with relatively stronger lateral density gradients (transect C) at four different scales: 2, 4, 8, and 16 km (Figs. 6a–d). As we progressively sharpen the filter width from 16 to 2 km, the vorticity field intensifies with the appearance of new filaments with $\zeta \sim f$ at the finer scales. Finescale features also emerge in the vorticity derived from the unfiltered velocity subsampled at the same scales above, confirming their presence is not an artifact of the filtering procedure. Repeating the above calculations for the other transects yields qualitatively similar results.

The vorticity in transect C between 25 and 30 km (Fig. 5f) is especially large ($\partial v/\partial x = 35f$). Analysis underway (J. Nash et al. 2018, unpublished manuscript) suggests the gradients in this particular region, with Rossby number $O(35)$, might be due to a nonlinear internal bore. These strong gradients occur across $O(1)$ m lateral scales and are confined to the top 10 m. The bulk of our analysis involves fields smoothed to $O(1)$ km scales and describes processes at $O(1$–$10)$ km scales over depths 8–40 m, the usable vertical range of the SADCP. For these reasons, we do not expect the bore to significantly impact our conclusions, and a

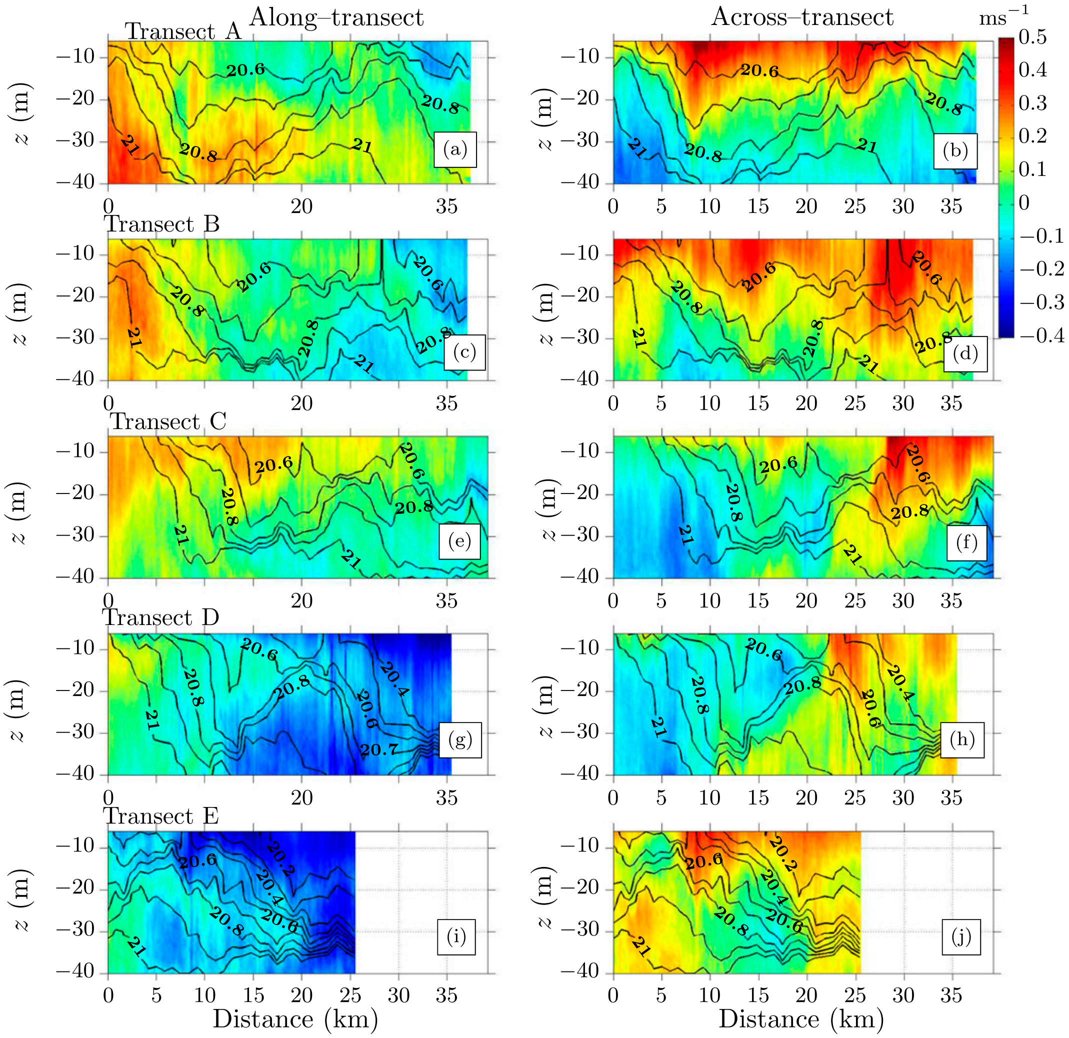

FIG. 5. Sections of the detided (no M_2 contribution) along-transect (u) and across-transect (v) velocities (m s^{-1}) from the SADCP, plotted as a function of the distance traveled by the ship. The x axis in all plots is oriented from southwest ($x = 0$ km) to northeast. The black lines denote isopycnal contours at intervals of 0.05 kg m^{-3}. The shallowest depth in all panels is 8 m.

fuller discussion of its dynamics is beyond the scope of this work.

We compute the skewness of the one-ship vertical vorticity field at an 8-km scale by merging the measurements from the entire survey (Fig. 6e). The skewness is positive between 8 and 40 m, peaking at 9 m with a maximum value of 0.87 and decreasing to 0.1 at 25 m. Estimating the mixed layer depth (MLD) H as the depth corresponding to a density increment of 0.2 kg m^{-3} from a depth of 1 m (Maneesha et al. 2012), yields an average value of 21 m for CBPS. Observations near deeper fronts show the skewness of ζ at $O(1)$ km scales peaks near the surface with a near-linear decrease toward zero over the depth of the mixed layer (Rudnick 2001; Shcherbina et al. 2013; Buckingham et al. 2016). Hence, the vertical variation of skewness at CBPS is qualitatively similar to that seen in earlier studies.

In summary, these calculations show ζ at $O(1)$ km scales is positively skewed, with the peak values scaling on f and intensifying at finer filter widths. The occurrence of $O(1)$ Rossby numbers ($\zeta \sim f$) could arise from both a sharp front in geostrophic balance and unbalanced motions. In the next section, we test the smoothed density and velocity fields for geostrophy.

b. Geostrophy

We use the velocity and density fields smoothed with an 8-km low-pass filter, wide enough to remove internal wave motions with $O(1)$ km or smaller wavelengths. We first construct a composite front out of the five transects

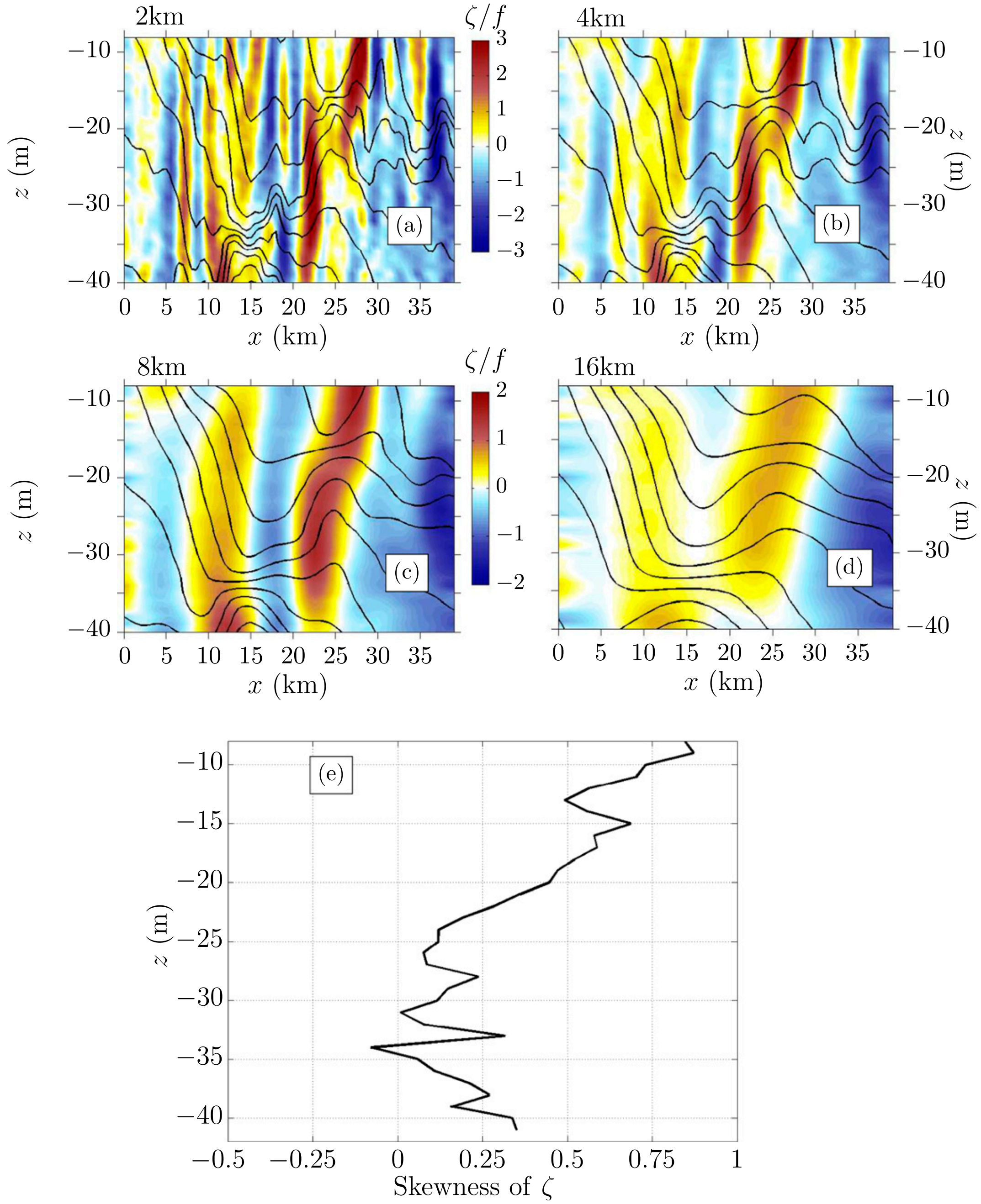

FIG. 6. Vertical vorticity, $\zeta \approx \partial v/\partial x$, scaled with the Coriolis parameter, for transect C, smoothed to four scales: (a) 2 km, (b) 4 km, (c) 8 km, and (d) 16 km. The color bar on top is for (a) and (b) while that below is for (c) and (d). The solid lines are isopycnals obtained from the UCTD measurements, spaced 0.05 kg m^{-3} apart and averaged to the same scale as the vorticity field in each panel. (e) Skewness of $\zeta \approx \partial v/\partial x$ at 8-km scale, obtained by merging data from the five transects at each depth.

as follows. Along each transect, we first locate the position where the magnitude of the lateral buoyancy gradient at the surface is maximum (Johnston et al. 2011). This procedure yields a location that alternates between one of the two clusters of outcropping fronts, depending on the transect. Therefore, to define the frontal axis consistently, we identify it with the cluster of fronts closer to the northern end along each transect. The locations of the frontal axis thus obtained are, from A to E, x_{FR} = (28, 28, 28, 27, 9) km. We then create the composite front by referencing the x coordinate of each transect to the corresponding x_{FR} and averaging

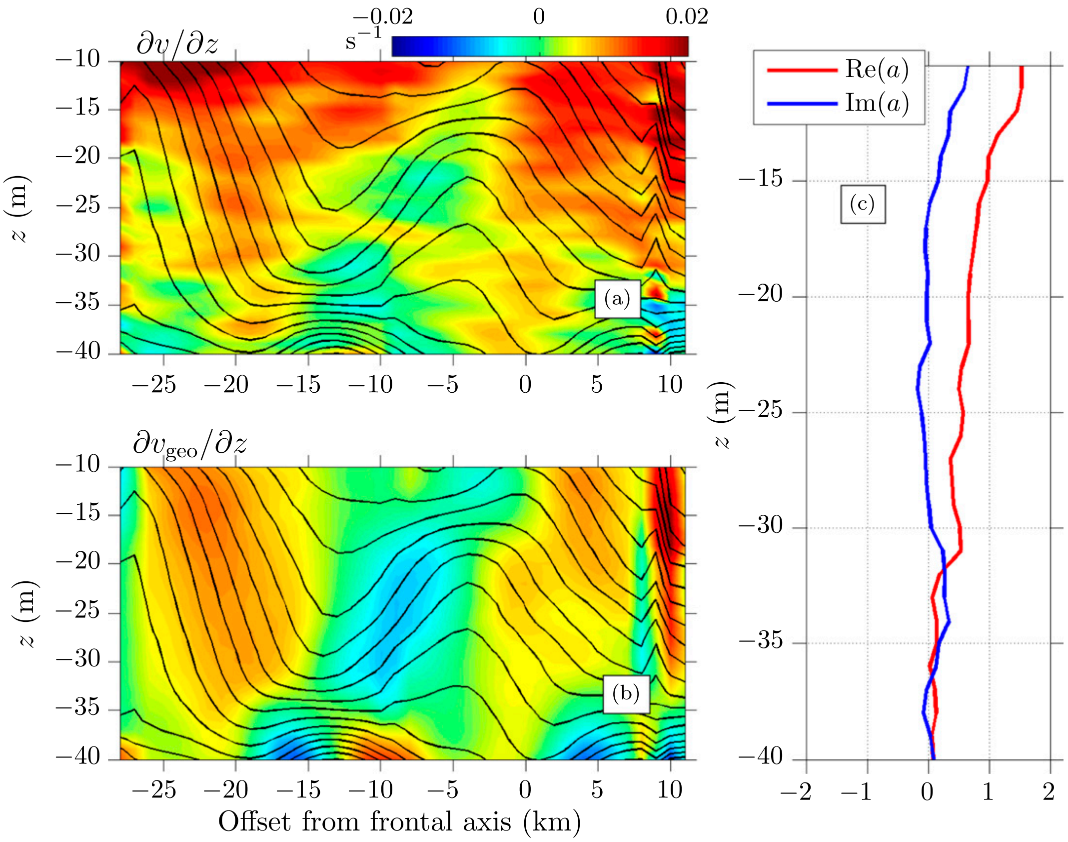

FIG. 7. (a) Vertical shear (s^{-1}) of the alongfront (orthogonal to the transect) velocity for the composite front, smoothed to 8 km. The abscissa is the distance along the transect referenced to the frontal axis. In the original coordinate system (Fig. 3), the locations of the frontal axis for the five transects are (28, 28, 28, 27, 9) km. (b) As in (a), but for the geostrophic component. (c) The slope of the linear regression between the observed shear and the thermal-wind shear for the entire radiator survey. Both observed and modeled shear are computed after filtering the velocity using an 8-km low-pass filter. Perfect geostrophy predicts the slope, $a = 1 + 0\iota$ [(2)], where $\iota^2 = -1$.

across the five transects. A visual comparison of $\partial v/\partial z$ and $\partial v_{\rm geo}/\partial z$ between $-40 < z < -10$ m for the composite front (Figs. 7a,b) shows some degree of spatial correlation between the two fields, suggestive of geostrophy.

To quantify our results, we test the thermal-wind relationship through a linear regression model between the observed vertical shear and the shear predicted by thermal-wind balance (Rudnick and Luyten 1996):

$$\overline{\mathbf{S}} = \frac{\iota a}{f}\left(\frac{\partial \overline{b}}{\partial x} + \iota\frac{\partial \overline{b}}{\partial y}\right), \qquad (1)$$

where $\mathbf{S} = \partial u/\partial z + \iota \partial v/\partial z$ is the complex velocity shear, $\iota^2 = -1$, a is the slope of the linear regression, and the overbar denotes a low-pass operation. From theory, the value of a that minimizes errors in a least squares sense is given by

$$a = -\iota f\frac{\langle \overline{\mathbf{S}}\nabla_h\overline{b}^*\rangle}{\langle \nabla_h\overline{b}\nabla_h\overline{b}^*\rangle}, \qquad (2)$$

where $\nabla_h = \partial/\partial x + \iota\partial/\partial y$ and the superscript asterisk denotes the complex conjugate. The angled brackets denote averaging along the transect. Geostrophy requires a to be purely real, that is, $a = 1 + \iota 0$. We attempt the regression by combining data from the five transects, as individual transects yield noisy results (Fig. 7c). The regression slope for the entire survey has a near-zero imaginary part for much of the water column between 15 and 40 m, but its real part is smaller than unity. A nearly real value of a with $|a| < 1$ reflects noise in the density signal, which amplifies the denominator in (2) without significantly modifying the correlation in the numerator (Rudnick and Luyten 1996). Above 15 m, the imaginary part of a is significant, conveying the importance of ageostrophic motions at those depths. This is consistent with the difference in the magnitudes of the observed and geostrophic shear for the composite front above 15 m. Hence, we interpret Fig. 7 as evidence for weak geostrophy at a scale of 8 km, between depths of 15 and 40 m. This weak balance allows us to use the velocity and density smoothed to 8 km as surrogate geostrophic fields while testing for various instabilities, taken up in the next section.

4. Lateral submesoscale processes at CBPS

In this section we present estimates of potential vorticity, followed by a comparison of the relative contributions from frictional and diabatic surface fluxes to PV averaged over the mixed layer. We then proceed to seek evidence for intimations of frontal instabilities at CBPS, using the fields at 8-km scale as a base state. We focus on the top 40 m, the region above the main pycnocline where the lateral variations in properties are the strongest.

a. *Ertel PV: Spatial structure*

The Ertel PV q is given by $q = (f\hat{\mathbf{k}} + \nabla\times\mathbf{u})\cdot\nabla b$, where $\hat{\mathbf{k}}$ is the unit vector in the vertical direction. Neglecting gradients orthogonal to the ship track yields the two-dimensional approximation

$$q \approx \left(f + \frac{\partial v}{\partial x}\right)N^2 - \frac{\partial v}{\partial z}M^2, \qquad (3)$$

where $M^2 \equiv \partial b/\partial x$. An estimation of the terms involving across-track gradients shows they are not likely to be significant for much of the survey, except for a portion of transect C between 8 and 10 km (appendix B), where the negative PV values near the surface occur during a period of solar warming and are suspect. The gradients in u orthogonal to the track might be significant in this region, thus invalidating (3) (appendix B).

We observe several patches with near-zero or negative values of q (Fig. 8). The vertical and lateral extent of these patches is $O(10)$ m and a few kilometers, respectively. The low-PV anomalies can be "baroclinically low" or "vortically low" Thomas (2008). The former results principally through large geostrophic shear at fronts, resulting in low q even if $(N^2, \zeta_{\mathrm{abs}}) \neq 0$, where $\zeta_{\mathrm{abs}} = \zeta + f$ is the absolute vorticity. Instances of baroclinically low PV are seen in several of the spatially coherent boluses with PV < 0, located at sharp fronts with nearly vertical isopycnals (Fig. 8), implying large M^2 but negligible N^2. These contrast the vortically low anomalies with low, but positive, q and weak (M^2, N^2). In these anomalies, low q in the absence of strong baroclinicity is achieved through negative ζ.

b. *Ertel PV: Frictional and diabatic surface fluxes*

The Eulerian evolution of the Ertel PV q is governed by the divergence of the PV flux vector $\mathbf{J}$ (Marshall and Nurser 1992):

$$\frac{\partial q}{\partial t} = -\nabla\cdot\mathbf{J}. \qquad (4)$$

The flux $\mathbf{J}$ combines contributions from advective and nonadvective processes. In this section, we estimate the vertical component of the latter at the surface. The nonadvective PV flux has two sources: (i) frictional forcing, namely, the interaction between winds and the surface lateral buoyancy gradient, and (ii) diabatic forcing arising from the exchange of heat at the air–sea interface. Denoting the vertical frictional and diabatic PV fluxes as J_z^{FRIC} and J_z^{DIAB}, respectively, they scale as (Thomas 2005)

$$J_z^{\mathrm{DIAB}} = c_1\frac{(f+\zeta)B_{\mathrm{net}}}{H}, \quad \text{and} \qquad (5)$$

$$J_z^{\mathrm{FRIC}} = c_2\frac{f\,\mathrm{EBF}}{H_{\mathrm{Ek}}}, \qquad (6)$$

where (c_1, c_2) are proportionality constants assumed here to be unity, B_{net} is the net buoyancy flux out of the ocean (W kg^{-1}), EBF is the Ekman buoyancy flux (W kg^{-1}), and H_{Ek} is the Ekman depth. The EBF is given by $\mathrm{EBF} = \mathbf{M}_e\cdot\nabla b|_{z=0}$, where $\mathbf{M}_e = \boldsymbol{\tau}\times\hat{\mathbf{z}}/(\rho_0 f)$ is the Ekman transport, $\boldsymbol{\tau}$ is the wind vector, $\hat{\mathbf{z}}$ is the unit vector in the local vertical direction, and ∇b is the horizontal buoyancy-gradient vector (Thomas et al. 2013). In terms of the individual wind stress components,

$$\mathrm{EBF} = \frac{1}{\rho_0 f}\left(\tau_y\frac{\partial b}{\partial x} - \tau_x\frac{\partial b}{\partial y}\right). \qquad (7)$$

Equation (7) shows winds with a downfront component result in a positive EBF and thus extract PV from the surface. In using (7), we neglect the term containing $\partial b/\partial y$ (justification in appendix B). The EBF is also sometimes expressed as an Ekman heat flux (W m^{-2}; Fig. 2b) $\mathrm{EHF} = [\rho_0 C_p/(\alpha g)]\mathrm{EBF}$, where α is the thermal expansion coefficient for seawater and $C_p = 3984\,\mathrm{J\,kg^{-1}\,{}^{\circ}C^{-1}}$ is the specific heat of seawater at constant pressure (Thomas 2005). In using (5), we replace ζ with f as we lack information about the vorticity field at the surface. Evaluating (5) with ζ at $z = -8$ m reduces slightly the injection of PV into the mixed layer during transects C and D. For the other transects, the rate of PV extraction is virtually indistinguishable from that obtained by setting $\zeta = f$ in (5).

Integrating (4) vertically over the mixed layer,

$$\frac{\partial}{\partial t}\langle q\rangle_H = \frac{1}{H}\int_{-H}^{0}\frac{\partial q}{\partial t} = -\frac{1}{H}(J_z^{\mathrm{DIAB}} + J_z^{\mathrm{FRIC}})\Big|_{-H}^{0} - \frac{1}{H}(\ldots), \qquad (8)$$

where $\langle\cdot\rangle_H$ denotes averaging over H. The parentheses in the final term on the right side of (8) represent

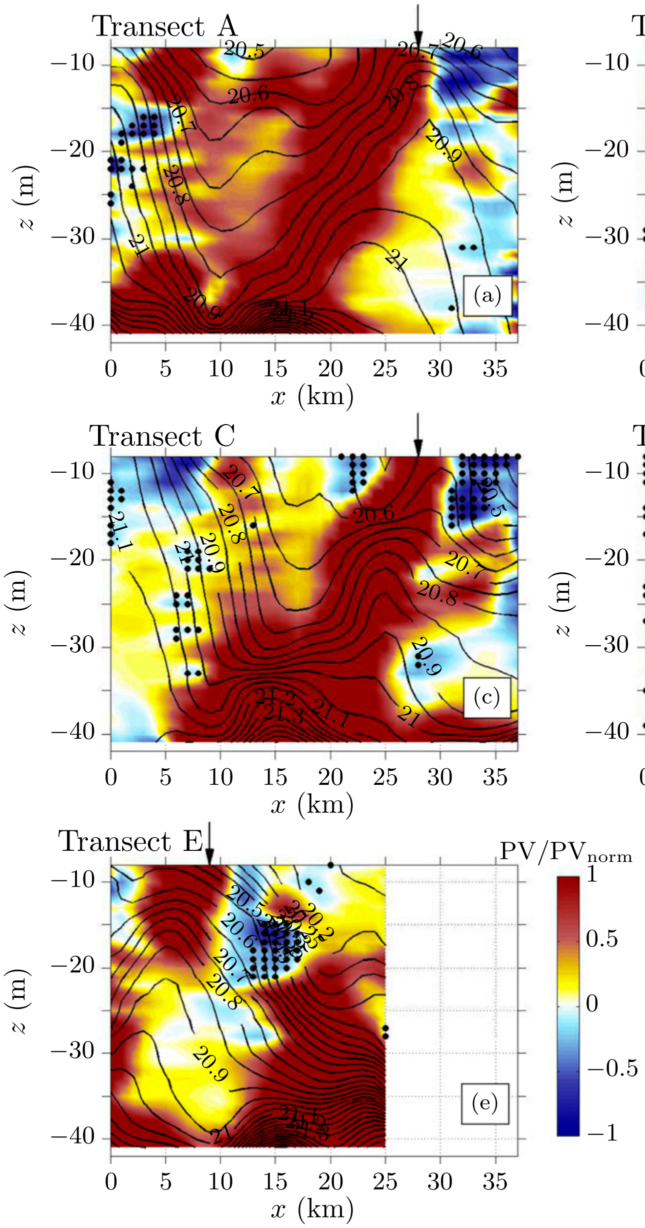

FIG. 8. The Ertel PV $(f\hat{\mathbf{k}} + \nabla \times \mathbf{u}) \cdot \nabla b$ (s^{-3}), obtained from the SADCP velocity and UCTD density fields smoothed to 8 km. The solid lines show isopycnals also smoothed to 8 km and contoured at intervals of 0.05 kg m^{-3}. The black dots identify locations where the flow satisfies the necessary conditions for FSI [(9), (10)]. The black arrows mark the location of the frontal axis.

advective and horizontal nonadvective PV fluxes integrated over the mixed layer. In using (8), we integrate q only from the mixed layer base up to a depth of 8 m because of noisy velocity data above this depth. We assume negligible frictional and diabatic PV fluxes at the mixed layer base $z = -H$, which is reasonable given the weak wind stress (Brainerd and Gregg 1993; Hosegood et al. 2008). The values of $\langle q \rangle_H$ become negative on several occasions, for instance, in transects A, B, C, and E (Fig. 9a). The negative values during the latter half of C are unreliable, as they could be a consequence of nonnegligible $\partial u/\partial y$ over that portion of the transect (appendix B). The EBF is mostly positive (Fig. 9b), indicating a predominantly downfront orientation of the winds. The magnitude of EBF is comparable with $B_{\rm net}$ despite weak winds, a testimony to the strong lateral density gradients in CBPS. In general, the contributions from EBF and $B_{\rm net}$ to the PV budget depend on the ratio $H/H_{\rm Ek}$ and need not be equal [(5) and (6)]. We obtain $H_{\rm Ek}$ from $H_{\rm Ek} = u_*/\sqrt{fN_m}$ (Pollard et al. 1972), where

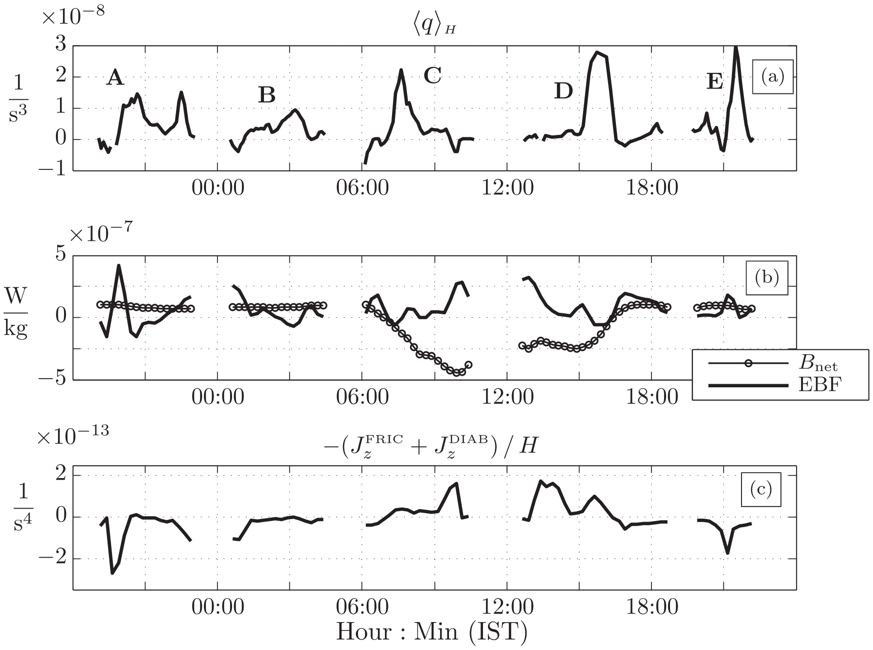

FIG. 9. (a) Ertel PV averaged over the mixed layer corresponding to an increment of $\Delta\rho = 0.2\,\mathrm{kg\,m^{-3}}$ from a depth of 1 m. (b) Net buoyancy flux at the ocean surface ($\mathrm{W\,kg^{-1}}$; line with circles), Ekman buoyancy flux ($\mathrm{W\,kg^{-1}}$) obtained from 15-min winds and the buoyancy field at a depth of 1 m, smoothed to 8 km. A positive flux indicates cooling of the ocean. (c) Contribution ($\mathrm{s^{-4}}$) from the diabatic and frictional flux to the PV budget averaged over the mixed layer.

N_m is the bulk stratification between 1 m and the mixed layer depth. The combined effect of J_z^{DIAB} and J_z^{FRIC} is mostly to extract PV, except when solar heating, through J_z^{DIAB}, injects PV into the mixed layer (Fig. 9c).

Integrating $-(J_z^{\mathrm{DIAB}} + J_z^{\mathrm{FRIC}})/H$ over the duration of transect A yields $-7.57 \times 10^{-10}\,\mathrm{s^{-3}}$, the PV extracted from the mixed layer. Bulk of the PV removal (69%) occurs during the sharp negative pulse in $-J_z^{\mathrm{NADV}}/H$ ($J_z^{\mathrm{NADV}} = J_z^{\mathrm{DIAB}} + J_z^{\mathrm{FRIC}}$), early in the transect (Fig. 9c). The time required to reduce $\langle q\rangle_H$ from zero to the peak negative value for A ($-4.15 \times 10^{-9}\,\mathrm{s^{-3}}$), assuming a transect-averaged rate of extraction $-\langle J_z^{\mathrm{NADV}}/H\rangle$ (Table 3), is approximately 20 h if we neglect the other terms in (8). The corresponding value using the average of J_z^{NADV} over the sharp negative pulse is 10 h. The other transects exhibit negative values in $\langle q\rangle_H$ comparable to those seen in A. The positive values in $\langle q\rangle_H$ for each of the transects are larger and $O(10^{-8})\,\mathrm{s^{-3}}$. Using a representative value of $1 \times 10^{-13}\,\mathrm{s^{-4}}$ for the positive divergence of the nonadvective PV flux during the heating phase (Fig. 9c), the time required to increase $\langle q\rangle_H$ by $O(10^{-8})\,\mathrm{s^{-3}}$ is 28 h. Hence, $-J_z^{\mathrm{NADV}}$ alone cannot generate the $O(10^{-8})\,\mathrm{s^{-3}}$ variability in $\langle q\rangle_H$ over the duration of a transect.

The depth-averaged contribution from the horizontal advective flux at 8-km scale, approximated here as $\langle -u\partial q/\partial x\rangle_H$, integrated over the transect is negative for all five transects. These estimates describe averages between the mixed layer base and 8 m. The magnitudes range from $O(10^{-10})\,\mathrm{s^{-3}}$ (for A, B, and D) to $O(10^{-9})\,\mathrm{s^{-3}}$ (for C and E). Thus, the lateral advective flux, as approximated here, is also incapable of generating $O(10^{-8})\,\mathrm{s^{-3}}$ variations in $\langle q\rangle_H$ over the duration of a transect.

To assess the potential contribution from the vertical advective PV flux, we approximate $\langle w\partial q/\partial z\rangle_H \approx \langle w\rangle_H \langle\partial q/\partial z\rangle_H$. Studies of shallow fronts in the California Current System with $|\nabla_h b| \sim 10^{-7}\,\mathrm{s^{-2}}$ and MLDs between 20 and 30 m report mesoscale vertical velocities reaching up to $10\,\mathrm{m\,day^{-1}}$, as predicted by the solutions to a generalized version of the ω equation (Pallàs-Sanz et al. 2010b). Estimating $\langle\partial q/\partial z\rangle_H$ using the difference in PV between 8 m and the mixed layer base and assuming $\langle w\rangle_H = 10\,\mathrm{m\,day^{-1}}$ yields contributions to PV ranging from $O(10^{-10})\,\mathrm{s^{-3}}$ (for B and E) to $O(10^{-9})\,\mathrm{s^{-3}}$ (for A, C, and D). These numbers are comparable to the modification of $\langle q\rangle_H$ by nonadvective and lateral advective fluxes. The above exercise, though crude, offers plausible estimates of the change in $\langle q\rangle_H$ due to $\langle w\rangle_H\langle\partial q/\partial z\rangle_H$. The calculations in this section, therefore, show the temporal changes in $\langle q\rangle_H$ at 8-km scale occur over time scales considerably longer than the duration of individual transects.

TABLE 3. The second column is contribution from nonadiabatic vertical fluxes to the PV averaged over the mixed layer and smoothed to 8 km. The third to fifth columns show rate of generation of N^2 averaged between depths of 3 and 35 m (except frontogenesis term) integrated over the duration of the transect by frontogenesis (8–35 m), frictional processes, and diabatic processes. The sixth column is the sum of the previous three columns. The seventh column lists observed stratification averaged over 3–35 m and over the transect. Numbers in columns 3–7 are obtained from fields smoothed to 2.1 km (equivalent to 15 min assuming an average ship speed).

Transect	$\int -(J_{\mathrm{NADV}}/H)\,dt$ (s^{-3})	$\Delta N^2_{\mathrm{FRONT}}$ (s^{-2})	$\Delta N^2_{\mathrm{FRIC}}$ (s^{-2})	$\Delta N^2_{\mathrm{DIAB}}$ (s^{-2})	Sum (s^{-2})	$\langle N^2_{\mathrm{OBS}}\rangle$ (s^{-2})
A	-7.57×10^{-10}	2.3×10^{-6}	-1.59×10^{-6}	-2.25×10^{-6}	-1.54×10^{-6}	1.18×10^{-4}
B	-3.45×10^{-10}	-3.66×10^{-6}	-1.81×10^{-6}	-1.45×10^{-6}	-6.92×10^{-6}	1.02×10^{-4}
C	4.78×10^{-10}	-1.44×10^{-5}	-3.33×10^{-6}	4.47×10^{-6}	-1.33×10^{-5}	1.20×10^{-4}
D	7.48×10^{-10}	9.17×10^{-6}	-4.73×10^{-6}	4.54×10^{-6}	8.98×10^{-6}	1.26×10^{-4}
E	-4.27×10^{-10}	1.51×10^{-5}	-1.08×10^{-6}	-1.35×10^{-6}	1.27×10^{-5}	1.93×10^{-4}

c. *Potential frontal instabilities at CBPS*

1) FORCED SYMMETRIC INSTABILITY

The atmospheric forcing at CBPS is conducive to the initiation of FSI because it extracts PV, through frictional and diabatic PV fluxes, for a significant part of the survey (Table 3). The time scales for generating the observed negative PV values, starting from a balanced state ($q = 0$), range from a few hours to nearly a day (section 4b). Strong winds, sometimes exceeding 0.2 N m^{-2}, marked the days leading up to CBPS, with the winds abating 24–28 h before the commencement of the survey. This suggests the prevalence of water with near-zero PV before CBPS, making the flow vulnerable to FSI in the presence of extractive PV fluxes. Moreover, it is plausible the earlier transects (A and B) had fluid with negative PV at the outset, given our estimated time scales for the removal of PV by nonadiabatic fluxes.

The conditions for FSI (Thomas et al. 2013) are expressed in terms of the angles $\phi_{\mathrm{Ri}_B} = \tan^{-1}[-M^4/(f^2N^2)]$ and $\phi_c = \tan^{-1}[-\zeta_{\mathrm{abs}}/f]$, where $\zeta_{\mathrm{abs}} = \zeta_g + f$ denotes the vertical component of the absolute geostrophic vorticity (the subscript g represents geostrophy). The conditions differ for cyclonic and anticyclonic flows:

$$N^2, \zeta > 0: \quad -90^\circ < \phi_{Ri_B} < \phi_c; \quad \phi_c < -45^\circ, \quad \text{and} \tag{9}$$

$$N^2 > 0, \zeta < 0: \quad -90^\circ < \phi_{Ri_B} < -45^\circ; \phi_c > -45^\circ. \tag{10}$$

If, in addition to these conditions, there is extraction of PV from the water column by atmospheric forcing (frictional and diabatic), the flow is susceptible to FSI. We approximate ζ_g as ζ obtained from v smoothed to 8 km, consistent with a weak geostrophic balance at a scale of 8 km (Fig. 7). The flow satisfies the necessary conditions for FSI in several regions (black dots, Fig. 8). While isolated dots might just indicate noise, larger, spatially coherent clusters are clearly discernible. The locations of these clusters along the transects coincide with times when nonadiabatic fluxes extract PV at the surface ($J_z^{\mathrm{NADV}} > 0$).

It is illustrative to look at the balanced Richardson number, $\mathrm{Ri}_B = N^2f^2/M^4$, for transects A, B, and E where there is extraction of PV for the entire duration of the transect (Fig. 9c). The regions prone to FSI in CBPS are associated with $\mathrm{Ri}_B \sim O(1)$ (Fig. 10). In each of these transects, an extended region contiguous with the cluster of locations prone to FSI, but itself stable to FSI, has $1 < \mathrm{Ri}_B < 2$. This is conveyed by the wide spatial separation between the contours for $\mathrm{Ri}_B = 1$ and $\mathrm{Ri}_B = 2$ in regions where the PV is low. For A and B, we find such marginally stable regions when $0 < x < 10$ km for depths between 15 and 35 m. In E, they are present when $10 < x < 15$ km between depths 20 and 30 m. The marginally stable regions are up to 10 m thick and can have a lateral extent approaching 10 km. The presence of these regions with flow conditions close to neutral stability for FSI (Ri_B slightly larger than unity) in the vicinity of other regions where FSI might be active, is suggestive of the neutrally stable Ri_B resulting from earlier FSI events. The arguments presented above are not definitive evidence for FSI but strengthen the case for its occurrence.

2) INERTIAL INSTABILITY

Inertial instability requires negative gradients in absolute momentum (Haine and Marshall 1998), defined as $M_{\mathrm{abs}} = v + fx$, where x is the coordinate in the across-front direction, approximated here as parallel to the transect. All transects show $\partial M_{\mathrm{abs}}/\partial x$ attains negative values in numerous regions, as seen in representative plots for A and C (Figs. 11a,b). In most of these regions, both the frontal term and the vortical term [(3)] are negative, reducing the PV. This suggests the potential for hybrid symmetric/inertial instability (Thomas et al. 2013). Occasionally, however, the vortical term is strong while the frontal gradients are weak (Fig. 11b, lower-right corner; $30 < x < 37$ km), implying a

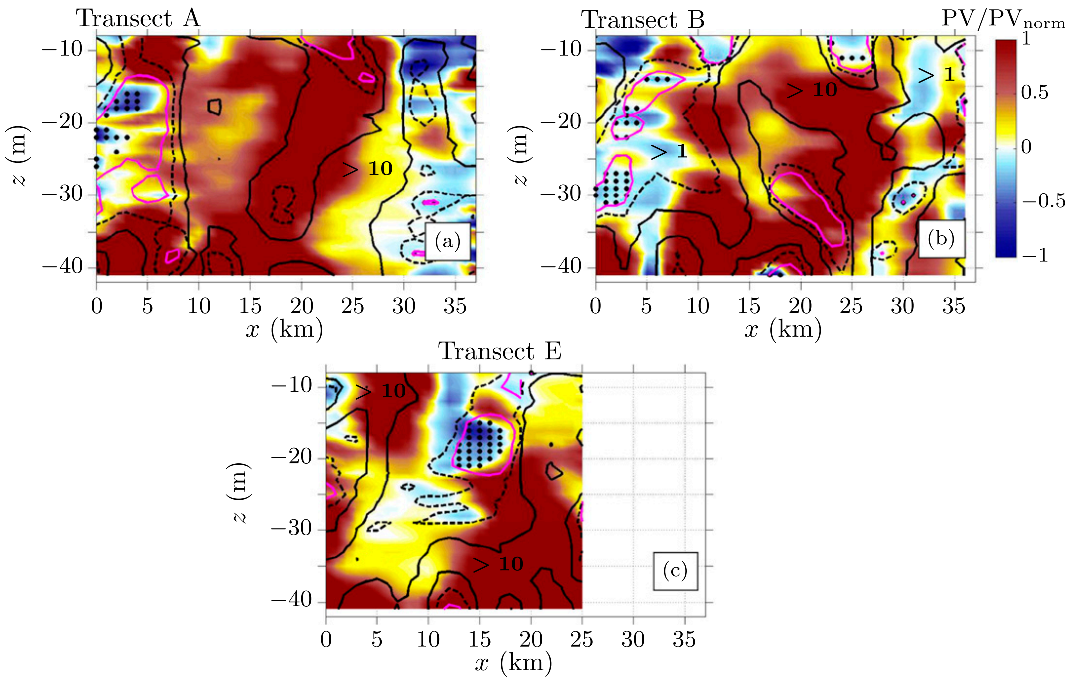

FIG. 10. (a) Normalized Ertel PV (color) for transect A. The contours of balanced Richardson number $\mathrm{Ri}_B = f^2N^2/M^4$ are shown for $\mathrm{Ri}_B = 1$ (magenta), 2 (dashed black), and 10 (solid black). The black dots identify locations where the flow conditions meet the necessary criteria for FSI [(9), (10)]. (b),(c) As in (a), but for transects B and E, respectively.

negligible contribution from $\partial b/\partial x$ to q [(3)]. Such circumstances convey the potential for inertial instability in its pure form.

3) AGEOSTROPHIC BAROCLINIC INSTABILITY

The wavelength and growth rate of the fastest-growing ABI mode are (Stone 1970)

$$L_{\mathrm{BI}} = \frac{2\pi U}{|f|}\sqrt{\frac{1+\mathrm{Ri}_B}{5/2}}, \quad \text{and} \tag{11}$$

$$T_{\mathrm{BI}} = \sqrt{\frac{54}{5}}\,\frac{\sqrt{1+\mathrm{Ri}_B}}{|f|}, \tag{12}$$

where U is a frontal velocity scale obtained by multiplying the transect-averaged values of geostrophic shear and H (Thompson et al. 2016). Using $\mathrm{Ri}_B = 1$ in (11) and (12) yields (from A to E) L_{BI} = (3.8, 10.1, 11.4, 15.35, 10.7) km. The time scale $T_{\mathrm{BI}} \approx 32$ h for all five transects as the change in latitude across transects is not significant.

Our analysis does not yield compelling evidence for the presence of ABI. It is possible the shallow mixed layers in CBPS inhibit the growth of energetic ABI modes. A second factor could be the short duration of the survey. Submesoscale-resolving simulations show ABI being the dominant instability after SI increases Ri_B to O(1). With conditions favoring the persistence of SI during CBPS (section 4b), aided by extractive PV fluxes at the surface, the estimated time scale for ABI modes suggests the survey might not have been long enough to witness ABI modes. Nevertheless, it is illustrative to consider the buoyancy flux ABI could generate, given the conditions at CBPS. The maximum buoyancy flux associated with restratification by ABI is $0.06\langle M^2\rangle_H^2 H^2/f$ (Fox-Kemper et al. 2008). We estimate this quantity using the 2-km buoyancy field because the parameterization requires M^2 describing a well-resolved submesoscale front. The resulting flux is often $O(10^{-7})$ W kg^{-1} with maximum values approaching 5.5×10^{-7} W kg^{-1} (Fig. 11). These values are comparable to B_{net} (Fig. 9b), implying similar flux divergences as the relevant vertical scale for both fluxes is H. These calculations suggest ABI, if active, is capable of generating buoyancy fluxes large enough to compete with the diabatic surface fluxes.

5. Vertical stratification at CBPS: Influence of vertical and lateral processes

In this section, we assess the relative influence of lateral and one-dimensional vertical processes in generating the stratification at CBPS. The motivations are twofold:

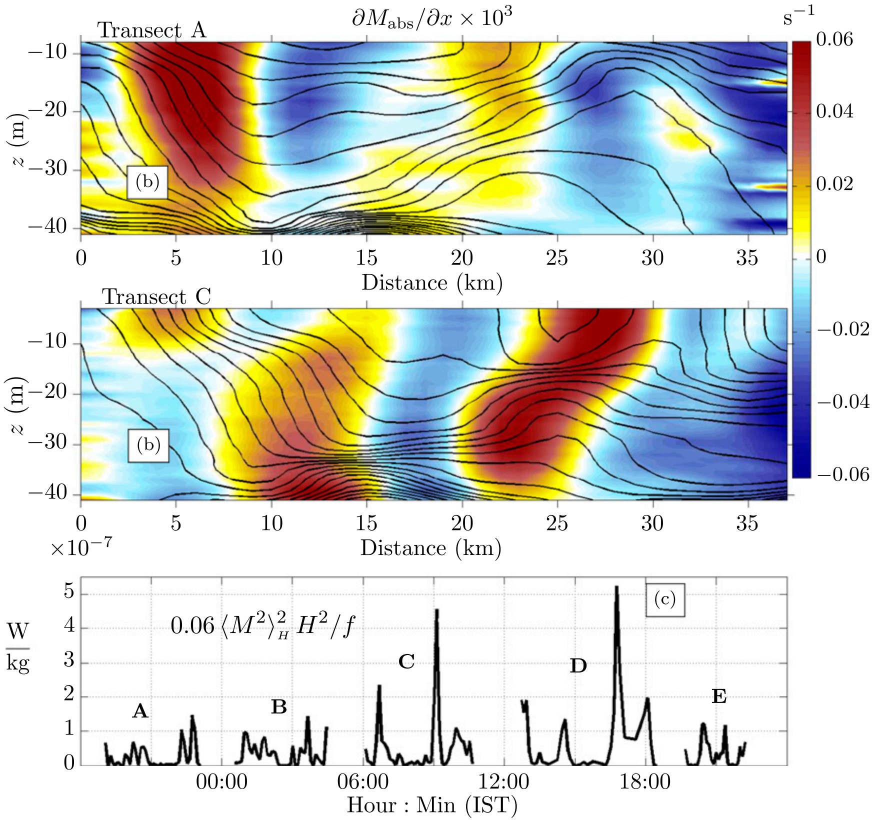

FIG. 11. (a) Gradient of absolute momentum $\partial M_{\rm abs}/\partial x = \partial v/\partial x + f$ ($\rm s^{-1}$; color) for transect A, from v smoothed to 8 km. The solid lines show isopycnals also smoothed to 8 km and contoured at intervals of 0.05 kg m^{-3}. Negative values (color) indicate conditions favorable for inertial instability. (b) As in (a), but for transect C. (c) Predicted maximum vertical buoyancy flux from the parameterization by Fox-Kemper et al. (2008), $0.06\langle M^2\rangle_H^2 H^2/f$, where the subscript H denotes averaging over the mixed layer.

(i) to show the lateral variability in N^2 cannot be explained by one-dimensional physics alone and (ii) to estimate the contribution from various mechanisms to the evolution of N^2.

a. Correlations between isopycnal thickness and vorticity on isopycnals

The isentropic PV (IPV; Hoskins 1985; Pollard and Regier 1992) is defined as follows:

$$\mathrm{IPV} = \frac{f+\zeta_\rho}{\Delta P}\frac{\Delta\rho}{\rho}, \qquad (13)$$

where $\zeta_\rho = (\partial v/\partial x - \partial u/\partial y)|_\rho$ is the "isentropic vorticity" evaluated on an isopycnal with density ρ and ΔP is the thickness (m) between the isopycnals $\sigma \pm \Delta\rho/2$. This formulation exposes correlations between isopycnal gradients and N^2, harder to infer from the Ertel PV (Fig. 8). As we show below, the presence of such correlations at CBPS illustrates clearly the imprint of lateral velocity gradients in the spatial variability of N^2.

We approximate (13) using only the contribution to isentropic vorticity from the along-track gradient. Following Pollard and Regier (1992), we compute the IPV by interpolating fields onto the five isopycnals, σ_t = (20.7, 20.8, 20.9, 21.0, 21.2) kg m^{-3}, and use $\Delta\rho = 0.1$ kg m^{-3}. The isopycnals occupy depths ranging from 5 to 50 m (Figs. 12, 13). The four shallowest isopycnals ($\sigma_t <$ 21.2 kg m^{-3}) outcrop into the surface layer, while the fifth and the deepest isopycnal (σ_t = 21.2 kg m^{-3}) does not (Fig. 3). We show results from transects A through D, as the results from E are not qualitatively different. For each transect, we calculate the frontogenesis function, IPV, isentropic vorticity, and the location of the isopycnal layers (0.1 kg m^{-3} thick) centered on each of the five chosen isopycnals. The frontogenesis function characterizes the growth rate of the magnitude of the lateral buoyancy gradient and is defined to be $\mathbf{Q}\cdot\nabla_h b$, where $\mathbf{Q} = -(\partial_x u \partial_x b + \partial_x v \partial_y b,\ \partial_y u \partial_x b + \partial_y v \partial_y b)$

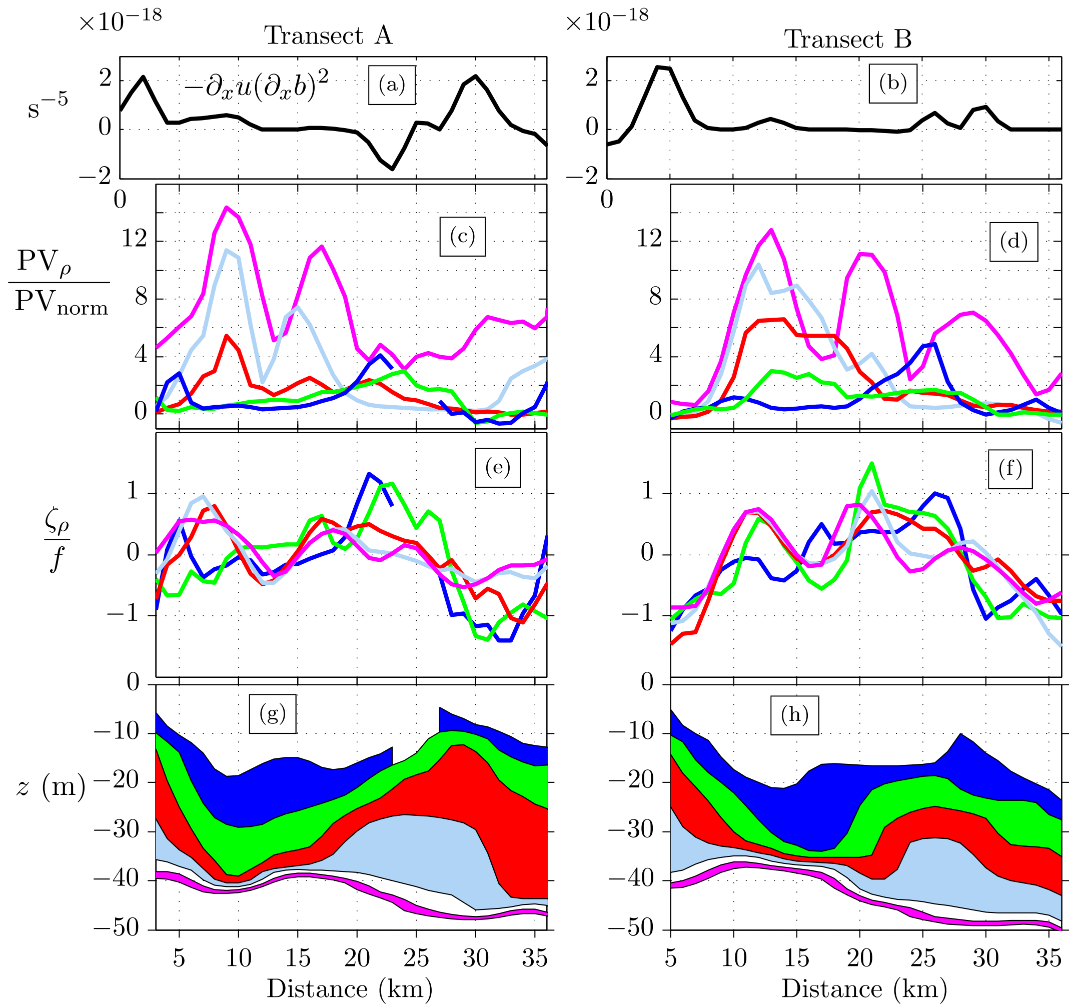

FIG. 12. (a),(b) Frontogenesis function (s^{-5}), approximated using only the along-transect gradients smoothed to 8 km. (c),(d) Normalized IPV along five isopycnals, $\sigma_t = 20.7, 20.8, 20.9, 21.0, 21.2\,\mathrm{kg\,m^{-3}}$, for transects A and B. The normalization factor is $6 \times 10^{-9}\,\mathrm{m^{-1}\,s^{-1}}$. (e),(f): Isentropic relative vorticity scaled with the Coriolis parameter. (g),(h) Thickness of isopycnal tubes bounded by $\sigma_t \pm 0.05\,\mathrm{kg\,m^{-3}}$, where σ_t attains the five values listed above. Spatial gaps in the tubes occur where the isopycnals outcrop. The limits on the x axis differ for the two transects.

(Hoskins 1982) and $\nabla_h b = (\partial_x b, \partial_y b)$. Considering only the along-transect gradients, $\mathbf{Q}\cdot\nabla_h b \approx -\partial_x u(\partial_x b)^2$, which we compute at a depth of 8 m as a proxy for surface frontogenesis, due to noisy velocity data at shallower depths. The IPV values for all five isopycnals are normalized with a common factor, $6 \times 10^{-9}\,\mathrm{m^{-1}\,s^{-1}}$. We first focus on transect A, before commenting on the others.

For the isopycnals $\sigma_t = (20.7, 20.8)\,\mathrm{kg\,m^{-3}}$, the normalized IPV (hereinafter IPV) is nearly zero or slightly negative in two regions: $5 < x < 15$ km and $27 < x < 33$ km (Fig. 12c). The left and right extremes of these two intervals, respectively, lie in the vicinity of strong frontogenetic forcing (Fig. 12a). For $5 < x < 15$ km, the IPV is small for the two shallowest isopycnals even though $\zeta_{\mathrm{abs},\rho} = \zeta_\rho + f \neq 0$, because the stratification is low (Figs. 12e,g). By contrast, the anomalously low IPV for $27 < x < 35$ km occurs alongside stronger stratification, where $\zeta_\rho = -f$ ensures the IPV stays close to zero. The isopycnals $\sigma_t = (20.9, 21.0)\,\mathrm{kg\,m^{-3}}$ also feature O(1–10)-km-long stretches of near-zero IPV toward the right edge of the transect. Similar low-IPV patches abound within other isopycnal layers above 40 m (not shown). The repeated occurrence of submesoscale, low-IPV "tubes" in the top 40 m, wherein ζ_ρ and the isopycnal thickness vary in lockstep to yield nearly constant low IPV, is a defining feature of CBPS and clear evidence one-dimensional vertical processes alone cannot reproduce the observed N^2. The properties on the $\sigma_t = 21.2\,\mathrm{kg\,m^{-3}}$ isopycnal contrast those on the

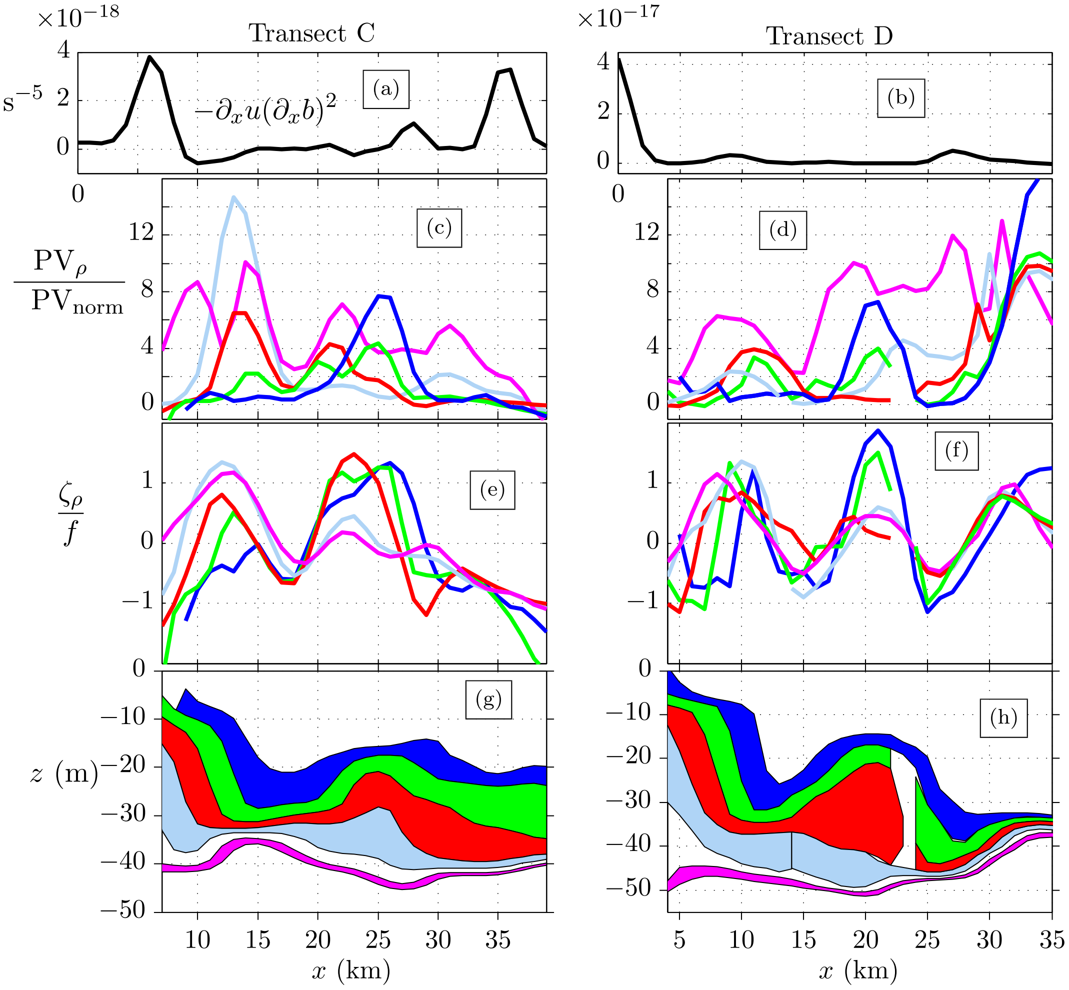

FIG. 13. As in Fig. 12, but for transects C and D. The limits on the x axis differ for the two transects.

outcropping isopycnals. The IPV on $\sigma_t = 21.2\,\text{kg}\,\text{m}^{-3}$ is typically much larger than on the other four isopycnals. This isopycnal also exhibits the least variations in isopycnal thickness, isentropic vorticity, and IPV. For instance, the IPV along the four shallowest isopycnals changes by an order of magnitude, but the corresponding change for $\sigma_t = 21.2\,\text{kg}\,\text{m}^{-3}$ is much smaller.

The above features are broadly replicated in the rest of CBPS (Figs. 12b,d,f,h, 13). In each transect, there are regions of constant IPV where the thickness between isopycnals and ζ_ρ mutually compensate each other. The low-IPV anomalies extend $O(1\text{–}10)$ km in length and are confined to the outcropping isopycnals in the top 40 m. Such anomalies are absent for the isopycnal $\sigma_t = 21.2\,\text{kg}\,\text{m}^{-3}$.

b. Solar heating

Among the five transects, only C and D were subject to solar heating. To estimate its contribution to N^2, we consider the divergence of the shortwave heat flux in the temperature tendency equation:

$$\left.\frac{\partial T}{\partial t}\right|_{\text{solar}} = -\frac{\partial F_s}{\partial z} = -\frac{1}{\rho_0 C_p}\frac{\partial}{\partial z}\left\{-|Q_{\text{sh}}|\left[R\exp\left(-\frac{z}{\xi_1}\right) + (1-R)\exp\left(-\frac{z}{\xi_2}\right)\right]\right\}, \qquad (14)$$

where Q_{sh} is the shortwave flux ($\text{W}\,\text{m}^{-2}$) at the ocean surface, R is the relative magnitude factor, ξ_1 is the attenuation length scale for radiation at long wavelengths (near infrared), and ξ_2 is the corresponding scale for short wavelengths (visible). The expression in square brackets is a double-exponential model for the penetrating downwelling irradiance, expressed as a fraction of its value at the surface (Paulson and Simpson 1977). Differentiating both sides with respect to z, switching the order of differentiation and converting to buoyancy units,

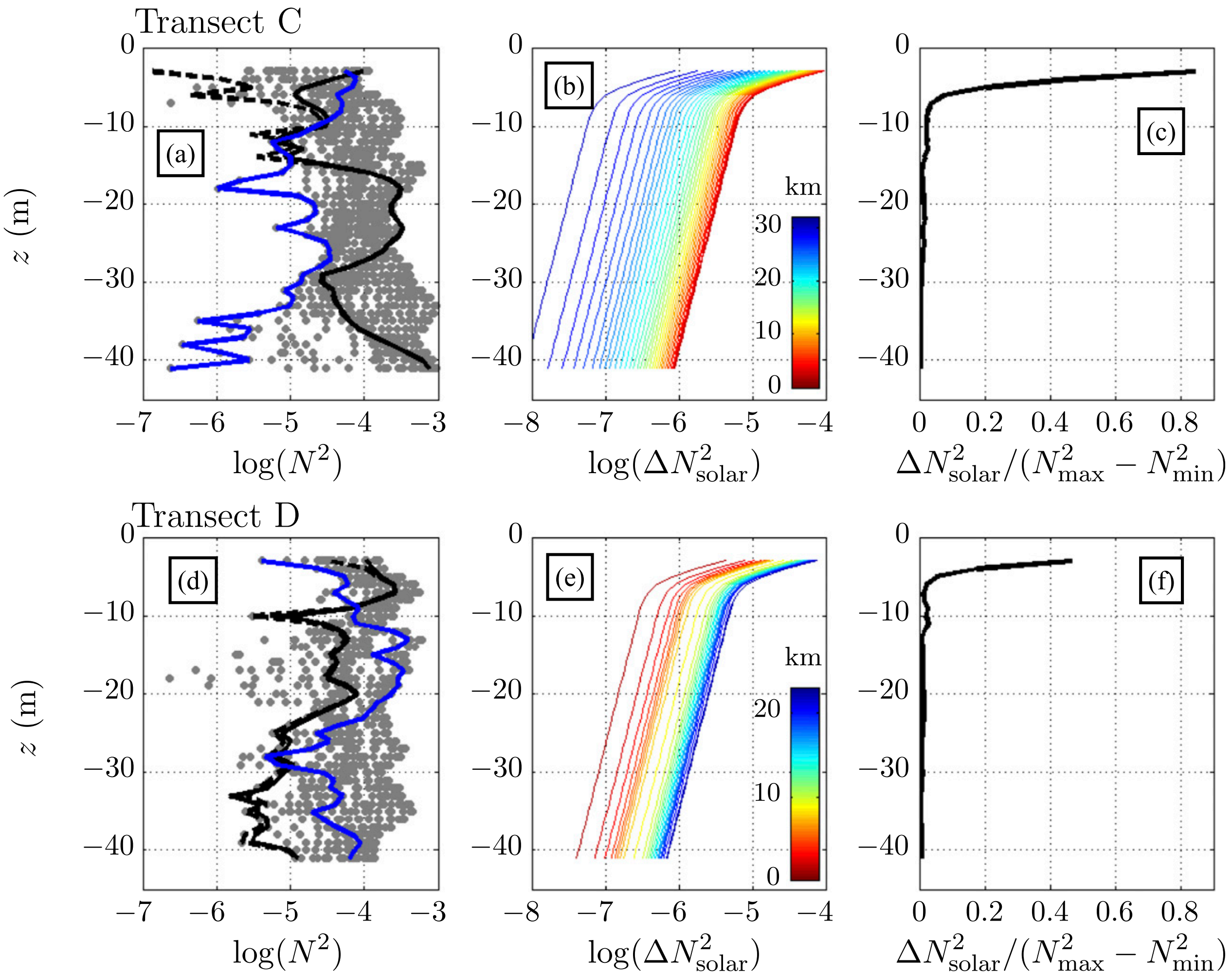

FIG. 14. (a) Gray dots represent N^2 (logarithmic scale, base 10) during the heating phase for transect C; black dashed line represents N^2 from UCTD at the commencement of heating; black solid line represents N^2 at the end of the heating phase due to solar insolation only, obtained by integrating (16) with the dashed line as the initial condition; and blue line represents N^2 from UCTD when the heating ends. (b) Increments in N^2 (logarithmic scale) calculated from (16). (c) Ratio of increase in N^2 from solar heating to the spread in N^2 (difference between maximum and minimum values) during the heating phase. (d)–(f) As in (a)–(c), but for transect D.

$$\frac{\partial}{\partial t}\left(g\alpha\frac{\partial T}{\partial z}\right)\bigg|_{\text{solar}} = \frac{g\alpha}{\rho_0 C_p}|Q_{\text{sh}}|\left[\frac{R}{\xi_1^2}\exp\left(-\frac{z}{\xi_1}\right) + \frac{(1-R)}{\xi_2^2}\exp\left(-\frac{z}{\xi_2}\right)\right]. \qquad (15)$$

Integrating (15) between times t_1 and t_2 provides the increase in stratification due to solar heating:

$$\Delta N^2(z)|_{\text{solar}} = \int_{t_2}^{t_2}\frac{g\alpha}{\rho_0 C_p}|Q_{\text{sh}}|\left[\frac{R}{\xi_1^2}\exp\left(-\frac{z}{\xi_1}\right) + \frac{(1-R)}{\xi_2^2}\exp\left(-\frac{z}{\xi_2}\right)\right]. \qquad (16)$$

We use $R = 0.4$, $\xi_1 = 0.9$ m, and $\xi_2 = 16$ m, values representative of wintertime conditions in the Bay for latitudes north of 15°N (Lotliker et al. 2016). For each of the transects C and D, we integrate (16) over the heating phase using $N^2(z)$ at the commencement of heating (black dashed line, Fig. 14a) as the initial condition. For C, a comparison of the observed N^2 at the end of the heating phase (blue line, Fig. 14a) with the corresponding prediction from (16) (black solid line, Fig. 14a) shows the influence of solar warming on N^2 is confined to the top 8 m. This is qualitatively consistent with rising temperatures very close to the surface (Fig. 3e) from $x = 25$ km toward $x = 0$ km, that is, in the direction of ship motion. Below this depth, the increment in N^2 due to Q_{sh} drops sharply (Figs. 14b,c) and contributes negligibly to the observed spread in N^2 during the heating phase (gray dots, Fig. 14a). Similar calculations for transect D show the effect of Q_{sh} on N^2 to be even less significant than for

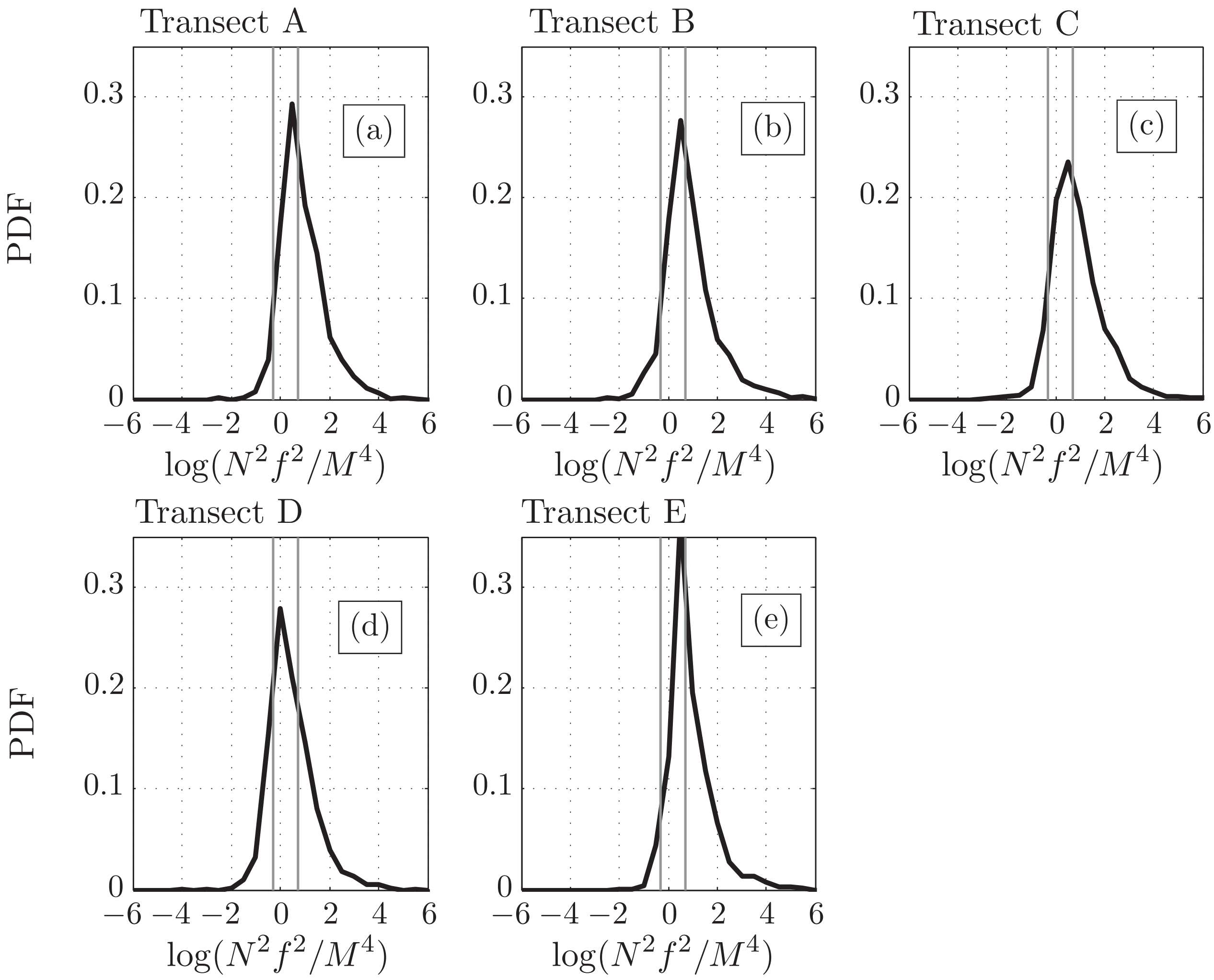

FIG. 15. PDFs of $\log(N^2f^2/M^4)$ within the top 40 m from UCTD fields smoothed to 8 km. The bin size is 0.5. The gray vertical lines are located at log(0.5) and log(5), indicating the band where $N^2f^2/M^4 \sim O(1)$. The ratios of (i) the area under the PDF, between the two lines [where $N^2f^2/M^4 \sim O(1)$], and (ii) the area under the PDF to the right of the line at log(0.5) [where $N^2f^2/M^4 \gtrsim O(1)$] are, from A to E, (0.51, 0.52, 0.51, 0.67, 0.54).

C (Figs. 14d–f). We conclude the contribution from solar warming to the observed variability in N^2 during the heating phase of CBPS is minor except within the top 8 m for part of transect C.

c. *Geostrophic adjustment*

An unforced front with vertical isopycnals tilts because of gravity, generating stratification as the front undergoes geostrophic adjustment. Under inviscid conditions, the isopycnals oscillate over one inertial period about their new, tilted mean position (Tandon and Garrett 1994). The maximum restratification thus possible is M^4/f^2. Probability distribution functions (PDFs) of $\log(N^2f^2/M^4)$ within the top 40 m (Fig. 15) are positively skewed with values much larger than those corresponding to $N^2f^2/M^4 \sim O(1)$ [i.e., values within the two vertical lines at log(0.5) and log(5)]. The ratios of (i) the area under the PDF between the two vertical lines [where $N^2f^2/M^4 \sim O(1)$] and (ii) the area under the PDF to the right of the line at log(0.5) [corresponding to $N^2f^2/M^4 \gtrsim O(1)$] are, from A to E, (0.51, 0.52, 0.51, 0.67, 0.54). Thus, for transect D, in 33% of the locations where $N^2f^2/M^4 \gtrsim O(1)$, the observed N^2 is significantly larger than what geostrophic adjustment alone can generate. In the remaining 67%, N^2 is consistent with geostrophic adjustment but could also arise from ageostrophic processes (like SI) that might increase N^2f^2/M^4 to $O(1)$ values (Taylor and Ferrari 2010).

d. *Rate of change of stratification due to frontogenetic and frictional processes*

In this section, we estimate the relative contributions from frontogenetic and frictional processes to the depth-averaged N^2 budget. The discussion below follows the framework outlined in Thomas and Ferrari (2008).

The evolution equation for N^2 is given by

$$\frac{\partial}{\partial t}N^2 = -\frac{\partial}{\partial z}(\mathbf{u}_h \cdot \nabla b) - \frac{\partial}{\partial z}\left(w\frac{\partial b}{\partial z}\right) + \frac{\partial D}{\partial z}, \qquad (17)$$

where $\mathbf{u}_h$ represents the horizontal velocity vector and $D \approx -B_{\mathrm{net}}/H$ represents diabatic forcing of buoyancy. Integrating (17) from the surface to some depth $z = -h$, we obtain,

$$\frac{\partial}{\partial t}\langle N^2\rangle_{-h} = -\frac{1}{h}(\mathbf{u}_h \cdot \nabla b)\Big|_{z=-h}^{z=0} - \frac{1}{h}\left(w\frac{\partial b}{\partial z}\right)\Big|_{z=-h}^{z=0} + \frac{1}{h}D\Big|_{z=-h}^{z=0}, \qquad (18)$$

where $\langle \ldots \rangle_{-h}$ denotes averaging over the depth h. From left to right, the contributions to the depth-averaged N^2 budget are differential sheared advection, vertical advection, and diabatic processes. The first term can be further split into

$$-\frac{1}{h}(\mathbf{u}_h \cdot \nabla b)\Big|_{z=-h}^{z=0} = -\frac{1}{h}(\mathbf{u}_{\mathrm{FT}} \cdot \nabla b)\Big|_{z=-h}^{z=0} - \frac{1}{h}(\mathbf{u}_{\mathrm{FR}} \cdot \nabla b)\Big|_{z=-h}^{z=0}, \qquad (19)$$

where $\mathbf{u}_{\mathrm{FT}}$ and $\mathbf{u}_{\mathrm{FR}}$ represent the nonfrictional and frictional contribution to $\mathbf{u}_h$, respectively. The effects of frontogenesis on stratification are contained in the first term on the right side of (19). The frictional term in (19) is related to the frictional PV flux J_z^{FRIC} as follows:

$$-\frac{1}{h}(\mathbf{u}_{\mathrm{FR}} \cdot \nabla b)\Big|_{z=-h}^{z=0} = -\frac{1}{fh}(J_z^{\mathrm{FRIC}})\Big|_{z=-h}^{z=0}. \qquad (20)$$

From (20), extractive PV fluxes at the surface ($J_z^{\mathrm{FRIC}} > 0$) decrease the column-averaged stratification. Using (19) and (20), we can evaluate the frictional and nonfrictional, that is, frontogenetic, contribution to differential sheared advection.

The frontogenetic term in (19) describes lateral straining of isopycnals by both submesoscale and mesoscale eddies. Because of the limited length of the transects (<40 km), the present dataset does not allow us to reliably separate the mesoscale and submesoscale contributions to frontogenesis. Nevertheless, it is illustrative to explore the effect of scale on the intensity of lateral straining by evaluating the terms in the depth-averaged N^2 budget at two scales: 2.1 km (Table 3) and 8 km (Table 4). The coarser scale describes submesoscale motions in weak geostrophic balance with $O(1)$ Rossby numbers (section 3b). The finer scale also describes submesoscale motions but further away from geostrophic balance. We first discuss the salient aspects at 2.1-km scale before commenting on the change of scale.

TABLE 4. As in columns 3 and 4 in Table 3, but at the 8-km scale. Numbers are expressed as percentage differences from the corresponding values in Table 3. The change in $\Delta N^2_{\mathrm{DIAB}}$ is less than 5%.

Transect	$\Delta N^2_{\mathrm{FRONT}}$ (%)	$\Delta N^2_{\mathrm{FRIC}}$ (%)
A	−9	−9
B	−46	5
C	−6	−3
D	209	25
E	8	16

(i) The change in N^2 due to each of the three terms is at least an order of magnitude smaller than the observed average N^2 during the transects. This implies the time scales over which these mechanisms modify N^2, on average, is much longer than the duration of the transect, consistent with our assumption of quasi-steady conditions in CBPS (section 2a).

(ii) The frictional term always tends to reduce the column-averaged N^2, as we expect for predominantly downfront winds.

(iii) For all transects, change in stratification due to differential sheared advection is the largest among the three terms. For transect E, it is an order of magnitude larger compared to the frictional and diabatic contributions. The effects of frontolysis and frontogenesis on the stratification, as conveyed by $\Delta N^2_{\mathrm{FRONT}}$, are comparable.

For coarser smoothing at 8 km, the change in $\Delta N^2_{\mathrm{FRIC}}$ varies from 25% for transect D to −9% for A. For transects A through C, $\Delta N^2_{\mathrm{FRONT}}$ is negative, which we interpret as reflecting the absence of frontogenesis and accompanying restratification at scales 2–8 km, now removed by the spatial filtering. Interestingly, for transect D, the restratification due to frontogenesis increases dramatically by 200% at the coarser scale. This suggests the presence of strong frontolysis at scales of 2–8 km in D that opposes frontogenesis by the larger, weakly balanced motions.

6. Discussion

a. *Balanced vs linear internal-wave motions*

The weak to moderate stratification in the upper 40 m throughout CBPS distinguishes it from sites of previous wintertime observations of submesoscale processes (see references in section 1), where the mixed layers were much deeper than those reported here. A vigorous internal-wave field in the stratified waters, if present, complicates the interpretation of lateral gradients evaluated at a fixed depth as characterizing weakly balanced submesoscale processes, because of contributions to the gradients from the heaving of isopycnals. We address these concerns below.

Among linear internal waves, the near-inertial band of frequencies is the most energetic in the upper ocean (Alford et al. 2016), energized primarily by winds, although recent observations report their spontaneous generation from frontal instabilities even under calm conditions (Alford et al. 2013; Nagai et al. 2015). The latter class of internal waves tends to have shorter horizontal wavelengths [$\sim O(10)$ km] compared to wind-generated near-inertial waves (NIWs) away from fronts (Alford et al. 2016). The uniformly weak wind stress during CBPS reduces the likelihood of local generation of wind-driven NIWs during the survey. Furthermore, the short sampling times preclude significant contamination of the gradients due to temporal variability of such motions, regardless of whether they are advected into the experimental site or initiated locally during the experiment. The bulk of our analysis involves gradients on a 1-km grid. Hence, even the shorter O(10) km NIWs, if present, are not likely to contribute significantly to the lateral spatial gradients in our analysis.

The skewness of ζ is positive and increases toward the surface (section 3a), a feature incompatible with an isotropic linear internal-wave field, which cannot generate a skewed vorticity distribution. Earlier modeling and observational studies of upper-ocean fronts have also reported a positive skewness for ζ (Rudnick 2001; Shcherbina et al. 2013). Linear internal waves can have skewed vorticity distributions due to strongly directional effects, as is the case near sites of internal-wave generation, for example, topography. We do not expect such effects to be prominent near the surface.

Fluctuations in the potential vorticity field can be used to infer the relative dominance of geostrophic and linear internal-wave motions (Kunze and Sanford 1993). Splitting each term comprising the PV [(3)] into an along-transect mean and a corresponding fluctuation, the linear Ertel PV anomaly is $fb'_z + \zeta'\langle N^2\rangle$, where the angled brackets denote the along-transect mean and the prime denotes fluctuations about this mean. For linear internal waves, this anomaly is zero as the two terms have opposite phase (Kunze and Sanford 1993). For geostrophic motions, the terms are in phase. Hence, for linear internal waves to dominate the signal, we expect the fluctuation level of the anomaly to be smaller than that of either of the two terms fb'_z or $\zeta'\overline{N^2}$. A comparison of the root-mean-square (rms) value of $fb'_z + \zeta'\overline{N^2}$ with that of each constituent term (not shown) between depths of 8 and 40 m shows the rms value of the sum is almost always larger than that of the individual terms. The results from this calculation do not change significantly for smoothing scales from 2 to 8 km. In summary, the arguments presented above suggest it is unlikely linear internal waves are a significant driver of the spatial variability at $O(1)$ km scales observed during CBPS.

b. *Results from prior LES studies modeled on CBPS*

Recent three-dimensional LES studies of idealized, shallow, unforced fronts initialized with parameters based on the conditions at CBPS (Sarkar et al. 2016) show the presence of SI. The initial density field, stable to Kelvin–Helmholtz instability, is in geostrophic balance with constant lateral and vertical stratification. Initially, $M^2/f^2 = 50$, toward the lower end of the range of values (50–800) in CBPS. The balanced front goes unstable primarily through SI, followed by secondary Kelvin–Helmholtz instability and turbulent mixing. The mixing is patchy, causing the initially uniform M^2 and N^2 to break down into alternating bands of weak and elevated stratification (lateral and vertical). The weakly stratified layers thus formed are up to 10 m thick and a couple of kilometers wide in the cross-frontal direction (cross-frontal domain size = 4.1 km), smaller in extent than the N^2 anomalies during CBPS. The PV in these layers (in the LES) is anomalously low. While these simulations are unforced, we anticipate atmospheric forcing that removes PV from the water column will help sustain the above sequence for longer durations. It remains to be seen whether increasing the cross-frontal dimension in the LES would allow the N^2 (and PV) anomalies to assume larger spatial scales, as observed during CBPS. The onset of SI, preceding secondary Kelvin–Helmholtz instability and turbulent mixing, has also been observed in two-dimensional LES of an idealized midlatitude mixed layer front atop a pycnocline (Taylor and Ferrari 2009). The initial values of (N^2/f^2, M^2/f^2) in the two studies are (1250, 50) (Sarkar et al. 2016) and (900, 42) (mixed layer values; Taylor and Ferrari 2009). Sarkar et al. (2016) also report three-dimensional instability modes with along-frontal variability, absent by construction in the LES by Taylor and Ferrari (2009). In summary, the qualitative similarities between the dynamical signatures described in earlier sections and results from three-dimensional LES are encouraging, supporting the possibility for the occurrence of FSI during CBPS.

7. Conclusions

In the present work, we analyzed observations from a high-resolution frontal survey in the Bay of Bengal during the winter monsoon. Our results show several submesocale signatures in the velocity and density fields, illustrating an important role for lateral frontal processes at $O(1–10)$ km scales in the upper Bay.

The process-study site was located in the central Bay and characterized by sharp fronts in the top 40 m, embedded in stratified waters. During the study, the fronts were forced by weak, downfront winds and were subject to approximately one diurnal cycle of solar insolation. We identify numerous regions with negative Ertel PV in the top 40 m, spanning $O(1–10)$ km laterally and $O(10)$ m in the vertical direction. The flow conditions in some of these anomalies satisfy the necessary conditions for forced symmetric instability (Thomas et al. 2013), with nearby regions bearing the imprint of earlier occurrences of FSI. Several other locations in the survey are susceptible to inertial instability. Analysis of the PV on isopycnals shows an abundance of low-PV tubes in the top 40 m, $O(1–10)$ km long and $O(1–10)$ m thick. Within these tubes, the stratification and anticyclonic relative vorticity vary in concert to yield low PV over $O(1–10)$ km scales. Estimation of terms in the depth-averaged stratification budget (excluding vertical advection) shows differential sheared advection contributes at leading order. Together, these calculations show one-dimensional vertical processes alone cannot explain the observed stratification or its lateral variability between depths of 8 and 40 m. More broadly, our results convey how lateral submesoscale gradients might bear on the vertical structure of shallow fronts in the Bay.

Reproducing the correct stratification in the upper Bay remains a challenge for large-scale models that exhibit a deep MLD bias (Parekh et al. 2016). Such models predict excessive shear and unrealistically low stratification in the upper ocean. It remains to be seen if an accurate representation of submesoscale processes, presently unresolved in these models, might help mitigate some of these biases. Existing submesoscale parameterizations (Fox-Kemper et al. 2008), in their present form, do not fare as well in regions receiving a large influx of freshwater (Luo et al. 2016). Submesoscale-permitting simulations of shallow fronts representative of those studied here are necessary to delineate the dynamical character of submesoscale flows in the Bay of Bengal. We will undertake such efforts in a future study.

Acknowledgments. The authors thank the reviewers for their detailed and insightful comments that led to substantial improvements in the manuscript. S. Ramachandran acknowledges support from the National Science Foundation through award OCE 1558849 and the U.S. Office of Naval Research, Grants N00014-13-1-0456 and N00014-17-1-2355. A. Tandon acknowledges support from the U.S. Office of Naval Research, Grants N00014-13-1-0456 and N00014-17-1-2355. J. T. Farrar and R. A. Weller were supported by the U.S. Office of Naval Research, Grant N00014-13-1-0453, to collect the UCTD data and process the UCTD and shipboard meteorological data. S. Bigorre is thanked for his work on processing the UCTD data and computing the air–sea fluxes from the shipboard meteorological data. J. Nash, J. Mackinnon, and A. F. Waterhouse acknowledge support from the U. S. Office of Naval Research, Grants N00014-13-1-0503 and N00014-14-1-0455. E. Shroyer acknowledges support from the U. S. Office of Naval Research, Grants N00014-14-10236 and N00014-15-12634. A. Mahadevan acknowledges support from the U. S. Office of Naval Research, Grant N00014-13-10451. A. J. Lucas and R. Pinkel acknowledge support from the U. S. Office of Naval Research, Grant N00014-13-1-0489. S.R. is grateful to Jared C. Buckley at the University of Massachusetts Dartmouth for generating the CCAR image.

APPENDIX A

Removal of the Contribution from the Mode-1 M_2 Baroclinic Tide Using the Wirewalker

This section details the removal of the contribution from the M_2 internal tide to the temperature, salinity, density, and velocity fields using the wirewalker (Fig. A1).

Linear wave solutions from the wirewalker

Hovmöller plots of velocity from the WW (not shown) show a pronounced contribution from the baroclinic M_2 internal tide. The duration of the WW record is 84 h, that is, several M_2 cycles, enabling the isolation of the M_2 tidal component. A best-fit analysis of plane-wave solutions to the observations yields the following solutions describing the contribution from the mode-1 baroclinic M_2 tide to the horizontal velocities and the isopycnal displacement η_{M2}:

$$U_{\mathrm{M2}} = \mathrm{Re}\left\{\left(k_x + \frac{if}{\sigma k_y}\right)\frac{1}{k_H}U\exp[\imath 2\pi(k_x x + k_y y - 24\sigma t + \phi)]\right\}, \tag{A1}$$

$$V_{\mathrm{M2}} = \mathrm{Re}\left\{\left(k_y - \frac{if}{\sigma k_x}\right)\frac{1}{k_H}U\exp[\imath 2\pi(k_x x + k_y y - 24\sigma t + \phi)]\right\}, \tag{A2}$$

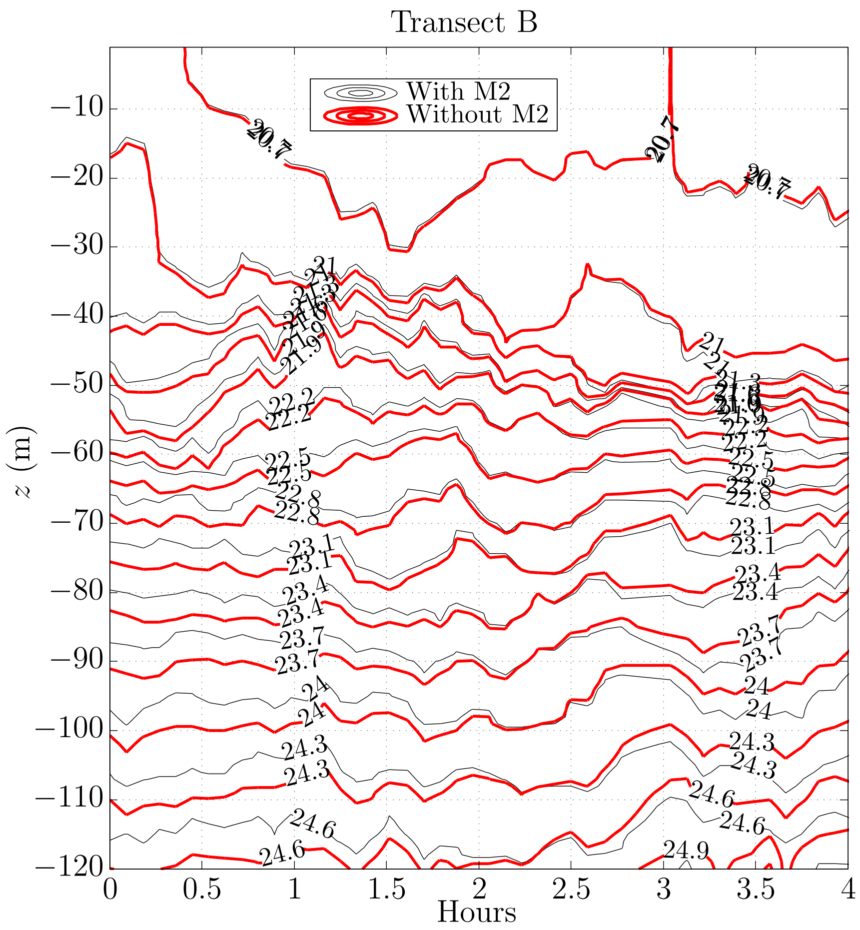

FIG. A1. CBPS, transect B, showing isopycnals before (black) and after (red) removing the contribution from the mode-1 M_2 baroclinic tide.

and

$$\eta_{\mathrm{M2}} = \mathrm{Re}\left\{Uz\frac{k_H}{\sigma}\frac{3600}{1000}\exp[\imath 2\pi(k_x x + k_y y - 24\sigma t + \phi)]\right\}, \qquad \text{(A3)}$$

where x and y are referenced to (16.2°N, 87.04°E), $U = 0.12\,\mathrm{m\,s^{-1}}$, $k_H = 0.008\,\mathrm{km^{-1}}$, $\theta = 180°$, $\phi = 20/360$, $\sigma = 1/12$ cph, $k_x = k_H\cos(\theta\pi/180)$, and $k_y = k_H\sin(\theta\pi/180)$.

We subtract the plane-wave solutions [(A1) and (A2)] from the velocity to get the M_2-detided fields. To obtain a density field from the M_2 solution for the isopycnal displacement, we assume the following relation between the observed density field ρ and the detided (no M_2 contribution) field ρ^d:

$$\rho = \rho^d + \frac{\partial\rho^d}{\partial z}(-\eta_{\mathrm{M2}}). \qquad \text{(A4)}$$

Equation (A4) is linear in η_{M2} and is the simplest expression of the effects of heaving isopycnals (due to the M_2 tide) on a background density field ρ^d, which we interpret here as the detided field and wish to solve for, through (A4). Discretizing (A4) using center-differencing for the vertical gradient yields,

$$\rho_k = \rho_k^d + \left(\frac{\rho_{k-1}^d - \rho_{k+1}^d}{2\Delta z}\right)[-\eta_{\mathrm{M2}}(z_k)], \qquad \text{(A5)}$$

where k indexes the levels in the vertical grid and increases from top to bottom. Using one-sided finite differencing at the top ($k = 1$) and bottom boundaries ($k = k_{\max}$) yields,

$$\rho_1 = \rho_1^d + \left(\frac{\rho_1^d - \rho_2^d}{\Delta z}\right)[-\eta_{\mathrm{M2}}(z_1)], \quad \text{and} \tag{A6}$$

$$\rho_{k_{\max}} = \rho_{k_{\max}}^d + \left(\frac{\rho_{k_{\max}-1}^d - \rho_{k_{\max}}^d}{\Delta z}\right)[-\eta_{\mathrm{M2}}(z_{k_{\max}})]. \tag{A7}$$

Rearranging the terms in (A5)–(A7) yields the linear system of equations $\mathbf{A}\mathbf{s}_1 = \mathbf{s}_2$, where the matrix $\mathbf{A}$ is given by

$$\mathbf{A} = \begin{pmatrix} 1 - \frac{\eta_{\mathrm{M2}}(z_1)}{\Delta z} & \frac{\eta_{\mathrm{M2}}(z_1)}{\Delta z} & 0 & \dots & \dots & \dots & 0 \\ -\frac{\eta_{\mathrm{M2}}(z_2)}{2\Delta z} & 1 & \frac{\eta_{\mathrm{M2}}(z_2)}{2\Delta z} & 0 & \dots & \dots & \vdots \\ 0 & \ddots & \ddots & \ddots & 0 & \dots & 0 \\ \vdots & \dots & \dots & 0 & -\frac{\eta_{\mathrm{M2}}(z_{k_{\max}-1})}{2\Delta z} & 1 & \frac{\eta_{\mathrm{M2}}(z_{k_{\max}-1})}{2\Delta z} \\ 0 & \dots & \dots & \dots & 0 & -\frac{\eta_{\mathrm{M2}}(z_{k_{\max}})}{\Delta z} & 1 + \frac{\eta_{\mathrm{M2}}(z_{k_{\max}})}{\Delta z} \end{pmatrix}, \tag{A8}$$

and the vectors $\mathbf{s}_1$ and $\mathbf{s}_2$ are given by $\mathbf{s}_1 = [\rho_1^d\, \rho_2^d \dots \rho_{k_{\max}}^d]^{\mathrm{T}}$, and $\mathbf{s}_2 = [\rho_1\, \rho_2 \dots \rho_{k_{\max}}]^{\mathrm{T}}$. Solving the tridiagonal system numerically provides ρ^d along the entire water column at a fixed location. Repeating the calculation throughout the transect yields ρ^d as a function of x and z. A comparison of ρ and ρ^d for transect B (Fig. A1) shows the tidal corrections can be as large as 5 m at a depth of 120 m but are insignificant in the top 40 m. A similar conclusion holds for the other transects as well.

Adapting (A4) for salinity, we obtain

$$\begin{aligned} S &= S^d + \frac{\partial S^d}{\partial z}(-\eta_{\mathrm{M2}}) \\ &= S^d + \frac{\partial S^d}{\partial \rho^d}\frac{\partial \rho^d}{\partial z}(-\eta_{\mathrm{M2}}) \\ &= S^d + \frac{1}{\beta\rho_0}\frac{\partial \rho^d}{\partial z}(-\eta_{\mathrm{M2}}), \end{aligned} \tag{A9}$$

where β is the saline contraction coefficient for seawater and $\rho_0 = 1027\,\mathrm{kg\,m^{-3}}$ is the reference density. Given ρ^d, it is straightforward to obtain S^d from (A9). A similar procedure yields the M_2 contribution to the temperature field. Figure A2 shows the temperature, salinity, and the two velocity components, without and with the M_2 contribution. Note the contributions to u and v from the M_2 tide are not insignificant (e.g., $0 < x < 5$ km).

APPENDIX B

Estimation of Contribution from Across-Track Gradients to the Ertel PV

In our approximation of the Ertel PV [(3)], we neglected gradients in buoyancy and velocity orthogonal to the transect. We first estimate potential errors from neglecting $\partial b/\partial y$, following the approach outlined in Thomas et al. (2016). The mean of the distribution of $\partial u/\partial z$ smoothed to 8 km, between depths of 8 and 40 m, is $5.95 \times 10^{-7}\,\mathrm{s^{-1}}$. Invoking thermal-wind balance, the contribution from the term involving $\partial b/\partial y$ is approximately $f\langle\partial u/\partial z\rangle^2$. The corresponding mean of the distribution of $\partial v/\partial z$ is $6 \times 10^{-3}\,\mathrm{s^{-1}}$. Hence, the contribution from $\partial b/\partial y$ to q is significantly smaller than that from $\partial b/\partial x$.

To estimate potential errors from the neglect of $\partial u/\partial y$, we approximate this gradient as the difference in u between successive transects divided by a representative distance separating the transects. Hence, $\zeta_{\mathrm{AB}} \approx (u_{\mathrm{B}} - u_{\mathrm{A}})/\Delta_{\mathrm{AB}}$ and so on for other pairs of transects. In this calculation, we use fields referenced to the frontal coordinates (section 3b). The location of the frontal axis changes only very slightly from A to D (x = 28, 28, 28, 27 km). For transects A and B, the corrections to q (in normalized PV units) where $q < 0$ are typically smaller than 0.1 (white space in

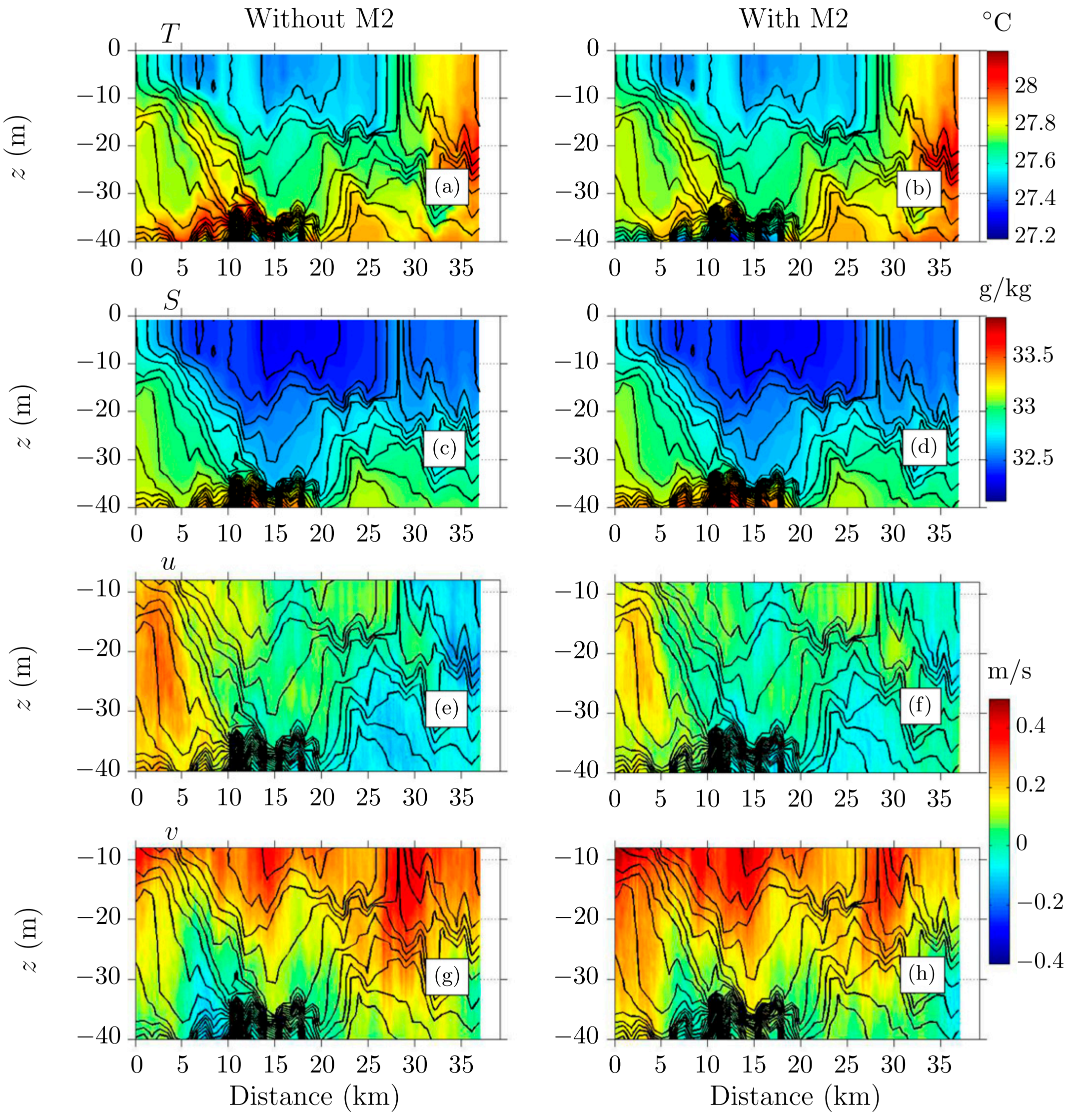

FIG. A2. CBPS, transect B, showing T, S, u, and v (left) without and (right) with the contribution from the mode-1 M_2 baroclinic tide. The solid lines are isopycnals contoured at 0.05 kg m^{-3}.

Figs. B1b,d shows values <0.1). In some regions the correction lies between 0.1 and 0.2 (near top-right corner in Fig. B1b), but the PV is sufficiently negative to remain negative. Occasionally, the corrections tend to make the PV more negative. The corrections are considerably larger for transect C, but are largest in regions that are not low-PV anomalies to begin with. We now consider some prominent low-PV anomalies in transect C on an individual basis. Near the top-left corner (Fig. B1e; $-25 < x < -20$ m), the positive corrections reach values larger than 0.5, overwhelming the negative values in the estimated PV. Within this region, the negative values of q should be viewed with caution. In the top-right corner, the PV is sufficiently negative to overcome the weakly positive corrections. In the bottom-right corner, the estimated PV and the corrections almost neutralize each other, leaving behind nearly zero PV values. For transect D, we estimate $\partial u/\partial y$ by approximately lining up D and E so that their right edges coincide (not shown). Within the strongly negative PV anomaly ($25 < x < 30$ km), we find a conservative estimate of the correction to PV that does not exceed 0.1 (PV units), but the estimated PV in the same region is negative with magnitudes larger than 0.1. For other low-PV (but positive) anomalies, the PV correction is negative or negligible. For transect E, we

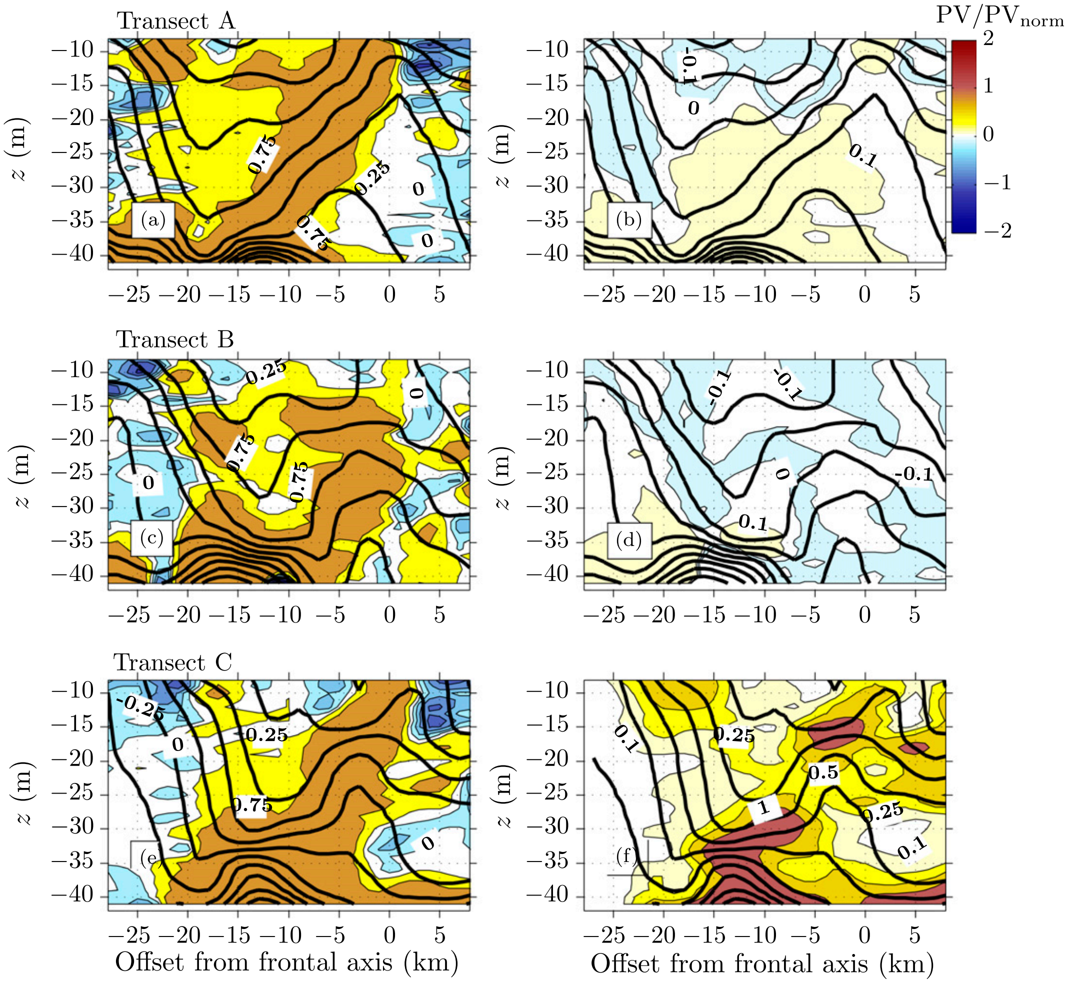

FIG. B1. CBPS showing estimation of contribution from across-track gradients in velocity to the Ertel PV smoothed to 8 km. Left panels show q (color and thin contours) from the one-ship approximation [(3)], normalized with $fN^2_{\rm av}$, where $N^2_{\rm av}$ is the stratification averaged over the length and depth (8–40 m) of the transect. The contour interval for negative values of the normalized PV is -0.25. For the positive values, only the 0.25 and 0.75 contours are shown. Right panels show the contribution from $\partial u/\partial y$ to q, normalized as above. In (b) and (d), the contour interval (thin lines) is 0.1. For (f), PV contours are marked at 0.1, 0.25, 0.5, 0.75, and so on. In all panels, the thick black contours represent potential density contoured at 0.1 kg m^{-3} for the earlier transect among the pair being considered [(a),(b) transect A; (c),(d) transect B; (e),(f) transect C].

merely note that the negative PV occurs in a strongly frontal region under conditions favorable to extraction of PV from the water column (Fig. 9c).

In summary, for much of the survey except for part of transect C, the contributions from the across-track gradients in u are not strong enough to erase the low anomalies in q obtained using the one-ship approximation.

REFERENCES

Alford, M. H., A. Y. Shcherbina, and M. C. Gregg, 2013: Observations of near-inertial internal gravity waves radiating from a frontal jet. *J. Phys. Oceanogr.*, **43**, 1225–1239, https://doi.org/10.1175/JPO-D-12-0146.1.

——, J. A. Mackinnon, H. L. Simmons, and J. D. Nash, 2016: Near-inertial internal gravity waves in the ocean. *Annu. Rev. Mar. Sci.*, **8**, 95–123, https://doi.org/10.1146/annurev-marine-010814-015746.

Arobone, E., and S. Sarkar, 2015: Effects of three-dimensionality on instability and turbulence in a frontal zone. *J. Fluid Mech.*, **784**, 252–273, https://doi.org/10.1017/jfm.2015.564.

Balaguru, K., P. Chang, R. Saravanan, L. R. Leung, Z. Xu, M. Li, and J.-S. Hsieh, 2012: Ocean barrier layers' effect on tropical cyclone intensification. *Proc. Natl. Acad. Sci. USA*, **109**, 14 343–14 347, https://doi.org/10.1073/pnas.1201364109.

Barkan, R., K. B. Winters, and S. G. L. Smith, 2015: Energy cascades and loss of balance in a reentrant channel forced by wind stress and buoyancy fluxes. *J. Phys. Oceanogr.*, **45**, 272–293, https://doi.org/10.1175/JPO-D-14-0068.1.

Benshila, R., F. Durand, S. Masson, R. Bourdallé-Badie, C. B. Montégut, F. Papa, and G. Madec, 2014: The upper

Bay of Bengal salinity structure in a high-resolution model. *Ocean Modell.*, **74**, 36–52, https://doi.org/10.1016/j.ocemod.2013.12.001.

Boccaletti, G., R. Ferrari, and B. Fox-Kemper, 2007: Mixed layer instabilities and restratification. *J. Phys. Oceanogr.*, **37**, 2228–2250, https://doi.org/10.1175/JPO3101.1.

Bonjean, F., and G. S. E. Lagerloef, 2002: Diagnostic model and analysis of the surface currents in the tropical Pacific Ocean. *J. Phys. Oceanogr.*, **32**, 2938–2954, https://doi.org/10.1175/1520-0485(2002)032<2938:DMAAOT>2.0.CO;2.

Brainerd, K., and M. C. Gregg, 1993: Diurnal restratification and turbulence in the oceanic surface mixed layer. Part I: Observations. *J. Geophys. Res.*, **98**, 22 645–22 656, https://doi.org/10.1029/93JC02297.

Buckingham, C. E., and Coauthors, 2016: Seasonality of submesoscale flows in the ocean surface boundary layer. *Geophys. Res. Lett.*, **43**, 2118–2126, https://doi.org/10.1002/2016GL068009.

Callies, J., R. Ferrari, J. M. Klymak, and J. Gula, 2015: Seasonality in submesoscale turbulence. *Nat. Commun.*, **6**, 6862, https://doi.org/10.1038/ncomms7862.

Capet, X., J. C. McWilliams, M. J. Molemaker, and A. F. Shchepetkin, 2008a: Mesoscale to submesoscale transition in the California Current System. Part I: Flow structure, eddy flux and observational tests. *J. Phys. Oceanogr.*, **38**, 29–43, https://doi.org/10.1175/2007JPO3671.1.

——, ——, ——, and ——, 2008b: Mesoscale to submesoscale transition in the California Current System. Part III: Energy balance and flux. *J. Phys. Oceanogr.*, **38**, 2256–2269, https://doi.org/10.1175/2008JPO3810.1.

Dai, A., and K. E. Trenberth, 2002: Estimates of freshwater discharge from continents: Latitudinal and seasonal variations. *J. Hydrometeor.*, **3**, 660–687, https://doi.org/10.1175/1525-7541(2002)003<0660:EOFDFC>2.0.CO;2.

D'Asaro, E., C. Lee, L. Rainville, R. Harcourt, and L. Thomas, 2011: Enhanced turbulence and energy dissipation at ocean fronts. *Science*, **332**, 318–322, https://doi.org/10.1126/science.1201515.

Fairall, C. W., E. F. Bradley, J. E. Hare, A. A. Grachev, and J. B. Edson, 2003: Bulk parameterization of air-sea fluxes: Updates and verification for the COARE algorithm. *J. Climate*, **16**, 571–591, https://doi.org/10.1175/1520-0442(2003)016<0571:BPOASF>2.0.CO;2.

Fekete, B. M., and C. J. Vörösmarty, 2002: High-resolution fields of global runoff combining observed river discharge and simulated water balances. *Global Biogeochem. Cycles*, **16**, 1042, https://doi.org/10.1029/1999GB001254.

Fox-Kemper, B., R. Ferrari, and R. W. Hallberg, 2008: Parameterization of mixed layer eddies. Part I: Theory and diagnosis. *J. Phys. Oceanogr.*, **38**, 1145–1165, https://doi.org/10.1175/2007JPO3792.1.

Gopalan, A. K. S., V. V. G. Krishna, M. M. Ali, and R. Sharma, 2000: Detection of Bay of Bengal eddies from TOPEX and *in situ* observations. *J. Mar. Res.*, **58**, 721–734, https://doi.org/10.1357/002224000321358873.

Haine, T. W. N., and J. C. Marshall, 1998: Gravitational, symmetric, and baroclinic instability of the ocean mixed layer. *J. Phys. Oceanogr.*, **28**, 634–658, https://doi.org/10.1175/1520-0485(1998)028<0634:GSABIO>2.0.CO;2.

Hamlington, P. E., L. P. V. Roekel, B. Fox-Kemper, K. Julien, and G. P. Chini, 2014: Langmuir–submesoscale interactions: Descriptive analysis of multiscale frontal spindown simulations. *J. Phys. Oceanogr.*, **44**, 2249–2272, https://doi.org/10.1175/JPO-D-13-0139.1.

Haney, S., B. Fox-Kemper, K. Julien, and A. Webb, 2015: Symmetric and geostrophic instabilities in the wave-forced ocean mixed layer. *J. Phys. Oceanogr.*, **45**, 3033–3056, https://doi.org/10.1175/JPO-D-15-0044.1.

Holton, J., 1992: *An Introduction to Dynamic Meteorology*. 3rd ed. Academic Press, 511 pp.

Hosegood, P. J., M. C. Gregg, and M. H. Alford, 2008: Restratification of the surface mixed layer with submesoscale lateral density gradients: Diagnosing the importance of the horizontal dimension. *J. Phys. Oceanogr.*, **38**, 2438–2460, https://doi.org/10.1175/2008JPO3843.1.

——, ——, and ——, 2013: Wind-driven submesoscale subduction at the north Pacific subtropical front. *J. Geophys. Res. Oceans*, **118**, 5333–5352, https://doi.org/10.1002/jgrc.20385.

Hoskins, B. J., 1974: The role of potential vorticity in symmetric instability and instability. *Quart. J. Roy. Meteor. Soc.*, **100**, 480–482, https://doi.org/10.1002/qj.49710042520.

——, 1982: The mathematical theory of frontogenesis. *Annu. Rev. Fluid Mech.*, **14**, 131–151, https://doi.org/10.1146/annurev.fl.14.010182.001023.

——, 1985: On the use and significance of isentropic potential vorticity maps. *Quart. J. Roy. Meteor. Soc.*, **111**, 877–946, https://doi.org/10.1002/qj.49711147002.

Johnston, T. M. S., D. L. Rudnick, and E. Pallàs-Sanz, 2011: Elevated mixing at a front. *J. Geophys. Res.*, **116**, C11033, https://doi.org/10.1029/2011JC007192.

Kumar, S. P., P. M. Muraleedharan, T. G. Prasad, M. Gauns, N. Ramaiah, S. N. de Souza, S. Sardesau, and M. Madhupratap, 2002: Why is the Bay of Bengal less productive during the summer monsoon compared to the Arabian Sea? *Geophys. Res. Lett.*, **29**, 1242, https://doi.org/10.1029/2001GL014530.

Kunze, E., and T. B. Sanford, 1993: Submesoscale dynamics near a seamount. Part I: Measurements of Ertel vorticity. *J. Phys. Oceanogr.*, **23**, 2567–2588, https://doi.org/10.1175/1520-0485(1993)023<2567:SDNASP>2.0.CO;2.

Leben, R. R., G. H. Born, and B. R. Engebreth, 2002: Operational altimeter data processing for mesoscale monitoring. *Mar. Geod.*, **25**, 3–18, https://doi.org/10.1080/014904102753516697.

Lee, T., G. Lagerloef, M. M. Gierach, H.-Y. Kao, S. Yueh, and K. Dohan, 2012: Aquarius reveals salinity structure of tropical instability waves. *Geophys. Res. Lett.*, **39**, L12610, doi:10.1029/2012GL052232.

Lotliker, A. A., M. M. Omand, A. J. Lucas, S. R. Laney, A. Mahadevan, and M. Ravichandran, 2016: Penetrative radiative flux in the Bay of Bengal. *Oceanography*, **29**, 214–221, https://doi.org/10.5670/oceanog.2016.53.

Luo, H., A. Bracco, Y. Cardona, and J. C. McWilliams, 2016: Submesoscale circulation in the northern Gulf of Mexico: Surface processes and the impact of the freshwater river input. *Ocean Modell.*, **101**, 68–82, https://doi.org/10.1016/j.ocemod.2016.03.003.

Mahadevan, A., and A. Tandon, 2006: An analysis of mechanisms for submesoscale vertical motion at ocean fronts. *Ocean Modell.*, **14**, 241–256, https://doi.org/10.1016/j.ocemod.2006.05.006.

——, L. Thomas, and A. Tandon, 2008: Comment on "Eddy/wind interactions stimulate extraordinary mid-ocean plankton blooms." *Science*, **320**, 448, https://doi.org/10.1126/science.1152111.

——, E. D. Asaro, C. Lee, and M. J. Perry, 2012: Eddy-driven stratification initiates North Atlantic spring phytoplankton blooms. *Science*, **337**, 54–58, https://doi.org/10.1126/science.1218740.

Maneesha, K., V. S. N. Murty, M. Ravichandran, T. Lee, W. Yu, and M. J. McPhaden, 2012: Upper ocean variability in the Bay of Bengal during the tropical cyclones Nargis and

Laila. *Prog. Oceanogr.*, **106**, 49–61, https://doi.org/10.1016/j.pocean.2012.06.006.

Marshall, J. C., and A. J. G. Nurser, 1992: Fluid dynamics of oceanic thermocline ventilation. *J. Phys. Oceanogr.*, **22**, 583–595, https://doi.org/10.1175/1520-0485(1992)022<0583:FDOOTV>2.0.CO;2.

McWilliams, J. C., and B. Fox-Kemper, 2013: Oceanic wave-balanced surface fronts and filaments. *J. Fluid Mech.*, **730**, 464–490, https://doi.org/10.1017/jfm.2013.348.

Molemaker, M. J., and J. C. McWilliams, 2005: Baroclinic instability and loss of balance. *J. Phys. Oceanogr.*, **35**, 1505–1517, https://doi.org/10.1175/JPO2770.1.

Nagai, T., A. Tandon, H. Yamazaki, and M. J. Doubell, 2012: Direct observations of microscale turbulence and thermohaline structure in the Kuroshio Front. *J. Geophys. Res.*, **117**, C08013, https://doi.org/10.1029/2011JC007228.

——, ——, E. Kunze, and A. Mahadevan, 2015: Spontaneous generation of near-inertial waves by the Kuroshio Front. *J. Phys. Oceanogr.*, **45**, 2381–2406, https://doi.org/10.1175/JPO-D-14-0086.1.

Pallàs-Sanz, E., T. M. S. Johnston, and D. L. Rudnick, 2010a: Frontal dynamics in a California Current System shallow front: 1. Frontal processes and tracer structure. *J. Geophys. Res.*, **115**, C12067, https://doi.org/10.1029/2009JC006032.

——, ——, and ——, 2010b: Frontal dynamics in a California Current System shallow front: 2. Mesoscale vertical velocity. *J. Geophys. Res.*, **115**, C12068, https://doi.org/10.1029/2010JC006474.

Parekh, A., J. S. Chowdary, O. Sayantani, T. S. Fousiya, and C. Gnanaseelan, 2016: Tropical Indian Ocean surface salinity bias in Climate Forecasting System coupled models and the role of upper ocean processes. *Climate Dyn.*, **46**, 2403–2422, https://doi.org/10.1007/s00382-015-2709-8.

Paulson, C. A., and J. J. Simpson, 1977: Irradiance measurements in the upper ocean. *J. Phys. Oceanogr.*, **7**, 952–956, https://doi.org/10.1175/1520-0485(1977)007<0952:IMITUO>2.0.CO;2.

Pinkel, R., M. A. Goldin, J. A. Smith, O. M. Sun, A. A. Aja, M. N. Bui, and T. Hughen, 2011: The Wirewalker: A vertically profiling instrument powered by ocean waves. *J. Atmos. Oceanic Technol.*, **28**, 426–435, https://doi.org/10.1175/2010JTECHO805.1.

Pollard, R. T., and L. A. Regier, 1992: Vorticity and vertical circulation at an ocean front. *J. Phys. Oceanogr.*, **22**, 609–625, https://doi.org/10.1175/1520-0485(1992)022<0609:VAVCAA>2.0.CO;2.

——, P. B. Rhines, and R. O. R. Y. Thompson, 1972: The deepening of the wind-mixed layer. *Geophys. Fluid Dyn.*, **4**, 381–404, https://doi.org/10.1080/03091927208236105.

Rao, R. R., and R. Sivakumar, 2003: Seasonal variability of sea surface salinity and salt budget of the mixed layer of the north Indian Ocean. *J. Geophys. Res.*, **108**, 3009, doi:10.1029/2001JC000907.

Rudnick, D. L., 2001: On the skewness of vorticity in the upper ocean. *Geophys. Res. Lett.*, **28**, 2045–2048, https://doi.org/10.1029/2000GL012265.

——, and J. R. Luyten, 1996: Intensive surveys of the Azores front. 1: Tracers and dynamics. *J. Geophys. Res.*, **101**, 923–939, https://doi.org/10.1029/95JC02867.

Sarkar, S., H. T. Pham, S. Ramachandran, J. D. Nash, A. Tandon, J. Buckley, A. A. Lotliker, and M. M. Omand, 2016: The interplay between submesoscale instabilities and turbulence in the surface layer of the Bay of Bengal. *Oceanography*, **29**, 146–157, https://doi.org/10.5670/oceanog.2016.47.

Sengupta, D., and M. Ravichandran, 2001: Oscillations of Bay of Bengal sea surface temperature during the 1998 summer monsoon. *Geophys. Res. Lett.*, **28**, 2033–2036, https://doi.org/10.1029/2000GL012548.

——, G. N. B. Raj, and S. S. C. Shenoi, 2006: Surface freshwater from Bay of Bengal runoff and Indonesian throughflow in the tropical Indian Ocean. *Geophys. Res. Lett.*, **33**, L22609, https://doi.org/10.1029/2006GL027573.

——, B. R. Goddalehundi, and D. S. Anitha, 2008: Cyclone-induced mixing does not cool SST in the post-monsoon north Bay of Bengal. *Atmos. Sci. Lett.*, **9**, 1–6, https://doi.org/10.1002/asl.162.

——, G. N. B. Raj, M. Ravichandran, and J. S. Lekha, 2016: Near-surface salinity and stratification in the north Bay of Bengal from moored observations. *Geophys. Res. Lett.*, **43**, 4448–4456, https://doi.org/10.1002/2016GL068339.

Shcherbina, A. Y., E. D'Asaro, C. M. Lee, J. M. Klymak, M. J. Molemaker, and J. C. McWilliams, 2013: Statistics of vertical vorticity, divergence and strain in a developed submesoscale turbulence field. *Geophys. Res. Lett.*, **40**, 4706–4711, https://doi.org/10.1002/grl.50919.

——, and Coauthors, 2015: The LatMix summer campaign: Submesoscale stirring in the upper ocean. *Bull. Amer. Meteor. Soc.*, **96**, 1257–1279, https://doi.org/10.1175/BAMS-D-14-00015.1.

Shetye, S. R., 1993: The movement and implications of the Ganges-Bramhaputra runoff on entering the Bay of Bengal. *Curr. Sci.*, **1**, 32–38, http://www.jstor.org/stable/24095547.

——, A. D. Gouveia, D. Shankar, S. S. C. Shenoi, P. N. Vinaychandran, D. Sundar, G. S. Michael, and G. Nampoothiri, 1996: Hydrography and circulation in the western Bay of Bengal during the northeast monsoon. *J. Geophys. Res.*, **101**, 14 011–14 005, https://doi.org/10.1029/95JC03307.

Stone, P. H., 1970: On non-geostrophic baroclinic stability: Part II. *J. Atmos. Sci.*, **27**, 721–726, https://doi.org/10.1175/1520-0469(1970)027<0721:ONGBSP>2.0.CO;2.

Tandon, A., and C. Garrett, 1994: Mixed layer restratification due to a horizontal density gradient. *J. Phys. Oceanogr.*, **24**, 1419–1424, https://doi.org/10.1175/1520-0485(1994)024<1419:MLRDTA>2.0.CO;2.

Taylor, J. R., and R. Ferrari, 2009: On the equilibriation of a symmetrically unstable front via a secondary shear instability. *J. Fluid Mech.*, **622**, 103–113, https://doi.org/10.1017/S0022112008005272.

——, and ——, 2010: Buoyancy and wind-driven convection at mixed layer density fronts. *J. Phys. Oceanogr.*, **40**, 1222–1242, https://doi.org/10.1175/2010JPO4365.1.

Thadathil, P., V. V. Gopalakrishna, P. M. Muraleedharan, G. V. Reddy, N. Araligidad, and S. Shenoy, 2002: Surface layer temperature inversion in the Bay of Bengal. *Deep-Sea Res.*, **49**, 1801–1818, https://doi.org/10.1016/S0967-0637(02)00044-4.

——, P. M. Muraleedharan, R. R. Rao, Y. K. Somayajulu, G. V. Reddy, and C. Revichandran, 2007: Observed seasonal variability of barrier layers in the Bay of Bengal. *J. Geophys. Res.*, **112**, C02009, https://doi.org/10.1029/2006JC003651.

Thomas, L. N., 2005: Destruction of potential vorticity by winds. *J. Phys. Oceanogr.*, **35**, 2457–2466, https://doi.org/10.1175/JPO2830.1.

——, 2008: Formation of intrathermocline eddies at ocean fronts by wind-driven destruction of potential vorticity. *Dyn. Atmos. Oceans*, **45**, 252–273, https://doi.org/10.1016/j.dynatmoce.2008.02.002.

——, and R. Ferrari, 2008: Friction, frontogenesis, and the stratification of the surface mixed layer. *J. Phys. Oceanogr.*, **38**, 2501–2518, https://doi.org/10.1175/2008JPO3797.1.

——, A. Tandon, and A. Mahadevan, 2008: Submesoscale ocean processes and dynamics. *Ocean Modeling in an Eddying Regime*, *Geophys. Monogr.*, Vol. 177, Amer. Geophys. Union, 217–228, https://doi.org/10.1029/177GM04.

——, C. M. Lee, and Y. Yoshikawa, 2010: The subpolar front of the Japan/East Sea. Part II: Inverse method for determining the frontal vertical circulation. *J. Phys. Oceanogr.*, **40**, 3–25, https://doi.org/10.1175/2009JPO4018.1.

——, J. R. Taylor, R. Ferrari, and T. M. Joyce, 2013: Symmetric instability in the Gulf Stream. *Deep-Sea Res. II*, **91**, 96–110, https://doi.org/10.1016/j.dsr2.2013.02.025.

——, ——, E. A. D'Asaro, C. M. Lee, J. M. Klymak, and A. Shcherbina, 2016: Symmetric instability, inertial oscillations, and turbulence at the Gulf Stream front. *J. Phys. Oceanogr.*, **46**, 197–217, https://doi.org/10.1175/JPO-D-15-0008.1.

Thompson, A. F., A. Lazar, C. Buckingham, A. C. N. Garabato, G. M. Damerell, and K. J. Heywood, 2016: Open-ocean submesoscale motions: A full seasonal cycle of mixed layer instabilities from gliders. *J. Phys. Oceanogr.*, **46**, 1285–1307, https://doi.org/10.1175/JPO-D-15-0170.1.

Timmermans, M.-L., and P. Winsor, 2013: Scales of horizontal density structure in the Chukchi Sea surface layer. *Cont. Shelf Res.*, **52**, 39–45, https://doi.org/10.1016/j.csr.2012.10.015.

Vinaychandran, P. N., V. S. N. Murty, and V. R. Babu, 2002: Observations of barrier layer formation in the Bay of Bengal during summer monsoon. *J. Geophys. Res.*, **107**, 8018, https://doi.org/10.1029/2001JC000831.

White, A. A., and R. A. Bromley, 1995: Dynamically consistent, quasi-hydrostatic equations for global models with a complete representation of the Coriolis force. *Quart. J. Roy. Meteor. Soc.*, **121**, 399–418, https://doi.org/10.1002/qj.49712152208.

Wijesekera, H. W., and Coauthors, 2016: ASIRI: An ocean–atmosphere initiative for Bay of Bengal. *Bull. Amer. Meteor. Soc.*, **97**, 1859–1884, https://doi.org/10.1175/BAMS-D-14-00197.1.